© 2021. Published by The Company of Biologists Ltd | Journal of Cell Science (2022) 135, jcs255026. doi:10.1242/jcs.255026

RESEARCH ARTICLE

SPECIAL ISSUE: CELL BIOLOGY OF LIPIDS

PDZD8-mediated lipid transfer at contacts between the ER and late endosomes/lysosomes is required for neurite outgrowth

Yuan Gao[1], Juan Xiong[2], Qing-Zhu Chu[1] and Wei-Ke Ji[1,*]

ABSTRACT

Membrane contact sites (MCSs) between the endoplasmic reticulum (ER) and late endosomes/lysosomes (LE/lys) are emerging as critical hubs for diverse cellular events, and changes in their extents are linked to severe neurological diseases. While recent studies show that the synaptotagmin-like mitochondrial-lipid-binding (SMP) domain-containing protein PDZD8 may mediate the formation of ER–LE/lys MCSs, the cellular functions of PDZD8 remain largely elusive. Here, we attempt to investigate the lipid transfer activities of PDZD8 and the extent to which its cellular functions depend on its lipid transfer activities. In accordance with recent studies, we demonstrate that PDZD8 is a protrudin (ZFYVE27)-interacting protein and that PDZD8 acts as a tether at ER–LE/lys MCSs. Furthermore, we discover that the SMP domain of PDZD8 binds glycerophospholipids and ceramides both *in vivo* and *in vitro*, and that the SMP domain can transport lipids between membranes *in vitro*. Functionally, PDZD8 is required for LE/lys positioning and neurite outgrowth, which is dependent on the lipid transfer activity of the SMP domain.

KEY WORDS: PDZD8, Endoplasmic reticulum, Late endosomes, Lysosomes, Membrane contact sites, Lipid transfer

INTRODUCTION

Endoplasmic reticulum (ER) and endosomes are two main organelles in the secretory and endocytic pathways. Besides vesicular transport, ER and endosomes can be linked via membrane contact sites (MCSs), microdomains at which the membranes of the ER and endosomes are closely apposed (with a gap of <30 nm) and tethered, and the extent of such contacts increases as endosomes mature (Friedman et al., 2013; Hönscher and Ungermann, 2014; King et al., 2020; Raiborg et al., 2015b; Cohen et al., 2018; Valm et al., 2017). The majority of early endosomes and all late endosomes and lysosomes (hereafter referred collectively to as LE/lys) are stably associated with the tubular ER network, and these contact sites represent long-lasting, stable tethering along the vast tubular ER membrane (Zajac et al., 2013). Thus, it is not surprising that ER–endosome MCSs play essential roles in cell physiology (Phillips and Voeltz, 2016; Wu et al., 2018).

To date, several cellular functions of ER–endosome MCSs have been unveiled. One such function is to enable dephosphorylation of endosomal epidermal growth factor receptor (EGFR) through ER-resident phosphatase PTP1B (Eden et al., 2010), while other ER–endosome MCSs can regulate endosome dynamics, including endosome trafficking along microtubules (MTs) and endosome division (Hoyer et al., 2018; Rowland et al., 2014; Zajac et al., 2013). Another fundamental function of these contact sites is to transfer lipids and ions between the opposing membrane of ER and endosomes (Phillips and Voeltz, 2016; van der Kant and Neefjes, 2014; Wu et al., 2018).

Although vesicular transport is considered as a major pathway for the transfer of lipids between bilayer membranes, this route can be bypassed by lipid transfer proteins (LTPs) that are often localized to MCSs (Scorrano et al., 2019; Wong et al., 2017). LTPs are able to extract lipids from a donor membrane, shield them from the aqueous cytosolic environment within their hydrophobic pockets, and subsequently deliver them to a target membrane. Besides transferring lipids, these LTPs always serve as molecular tethers that physically bridge two opposing organelles and attach them to each other to ensure high efficiency of lipid transfer (Gatta and Levine, 2017; Saheki and De Camilli, 2017). Multiple proteins are proposed as potential tethers at ER–endosome MCSs in metazoans, including ER-resident vesicle-associated membrane proteins (VAPs) (Murphy and Levine, 2016) and the ER transmembrane (TM) protein protrudin (ZFYVE27) (Raiborg et al., 2015a; Shirane and Nakayama, 2006), Star-related lipid transfer domain containing 3 (STARD3) (Alpy et al., 2013), and oxysterol-binding protein-related protein 1L (ORP1L; also known as OSBPL1A) (van der Kant et al., 2013) as well as vacuolar protein sorting-associated protein 13C (VPS13C) (Kumar et al., 2018). One important characteristic of ER–LE/lys MSCs is that such contact sites directly regulate LE/lys positioning. Protrudin plays critical roles in both formation of ER–LE/lys MCSs and LE/lys positioning (Raiborg et al., 2015a). The ER-resident protrudin directly binds Rab7a and phosphatidylinositol 3-phosphate (PI3P) to facilitate formation of transient ER–LE/lys MCSs. At such MCSs, protrudin delivers kinesin-1 to FYVE and coiled-coil domain containing 1 (FYCO1) on the LE/lys membrane, thus promoting anterograde transport of LE/lys. Protrudin-mediated ER–LE/lys MCSs are essential for neurite outgrowth through promoting LE/lys anterograde transport and subsequent fusion with plasma membrane (Raiborg et al., 2015a).

While recent studies have suggested that PDZD8 mediates the formation of the ER–LE/lys MCSs (Elbaz-Alon et al., 2020; Guillén-Samander et al., 2019; Shirane et al., 2020), the cellular functions of PDZD8 and the extent to which its cellular functions depend on lipid transfer activities are largely elusive. Consistent with recent studies, we demonstrated that PDZD8 interacted with protrudin, and that PDZD8 acted as a tether at ER–LE/lys MCSs (Elbaz-Alon et al., 2020; Guillén-Samander et al., 2019;

[1]Department of Biochemistry and Molecular Biology, School of Basic Medicine, Tongji Medical College, Huazhong University of Science and Technology, Wuhan, Hubei, 430030, China. [2]Department of Anesthesiology, Tongji Hospital, Tongji Medical College, Huazhong University of Science and Technology, Wuhan, Hubei, 430030, China.

*Author for correspondence (J_WK@HUST.EDU.CN)

Y.G., 0000-0002-3714-5540; J.X., 0000-0002-3005-0274; Q.-Z.C., 0000-0002-0574-8275; W.-K.J., 0000-0003-1788-0879

Handling Editor: Giampietro Schiavo
Received 30 September 2020; Accepted 17 February 2021

Journal of Cell Science (2022) 135, jcs255026. doi:10.1242/jcs.255026

Hirabayashi et al., 2017; Shirane et al., 2020). Furthermore, we discovered that the SMP domain of PDZD8 binds glycerophospholipids and ceramides both *in vivo* and *in vitro*, and can transport lipids between membranes *in vitro*. Functionally, PDZD8 is required for LE/lys positioning and neurite growth in a lipid transfer activity-dependent manner.

RESULTS

PDZD8 interacts with the TM domain of protrudin

To identify unknown proteins that may interact with protrudin, we performed GFP-Trap assays in COS7 cells transiently expressing GFP–protrudin followed by mass spectrometry (MS) analysis. After removal of those proteins co-immunoprecipitated (co-IPed) by GFP alone, we found multiple known protrudin-interacting proteins including VAPA, VAPB and Rab7a in the coIP-MS results (Fig. S1A). A SMP domain-containing protein named PDZ domain-containing protein 8 (PDZD8) strongly interested us owing to its potential lipid transfer activities (Fig. S1A). Therefore, we sought to explore the cellular localizations and functions of PDZD8.

To confirm the protrudin–PDZD8 interaction, we performed GFP-Trap assays using GFP–protrudin (Fig. 1A, top) or PDZD8–GFP as bait (Fig. 1A, bottom). Consistent with recent studies (Elbaz-Alon et al., 2020; Shirane et al., 2020), our GFP-trap assays confirmed the protrudin–PDZD8 interactions in both conditions. We further dissected the protrudin protein, and found that the TM domain (residues 1–208) of protrudin was responsible for interacting with PDZD8 (Fig. 1B). Note that PDZD8 did not interact with FYCO1 (Fig. S1B), a protrudin-interacting protein (Raiborg et al., 2015a). We could not produce purified PDZD8 from either human or other organisms in sufficient quantities for biochemical analysis. Thus, the direct interaction between PDZD8 and TM domain of protrudin could not be examined in this study. Since protrudin is enriched at ER–LE/lys MSCs (Raiborg et al., 2015a), we further examined whether PDZD8 colocalized with protrudin at these MCSs by live-cell confocal microscopy. We showed that PDZD8–Halo indeed colocalized with GFP–protrudin (Pearson's correlation coefficient=0.83) (Fig. 1C). The colocalization could be observed not only along ER tubules (Fig. 1C, box 1) but also on LE/lys, likely at the ER-LE/lys MSCs (Fig. 1C, box 2). However, we noted that small interfering RNA (siRNA)-mediated suppression of PDZD8 did not inhibit the enrichment of protrudin on LE/lys, indicating that the localization of protrudin to such MCSs is independent of PDZD8 (Fig. S1C–E).

PDZD8 localizes to ER–LE/lys MCSs

To explore the role of PDZD8 at MCSs, we started with examination of its cellular localization in animal cells. To avoid the artifacts of cytomegalovirus promoter (CMV)-driven high expression in imaging, we generated a stable single clone COS7 cell line (hereafter referred to as sPDZD8-GFP) that was infected with a lentiviral vector for PDZD8–GFP expression driven by the weak promoter EF1α, which showed a lower and more homogeneous expression level of PDZD8–GFP compared to CMV promoter-driven transient expression, as revealed by flow cytometry analysis (Fig. S1F). We then investigated the cellular localization of PDZD8 in the sPDZD8-GFP line transiently expressing Lamp1–Halo as a LE/lys marker, ER-tagRFP as an ER marker, and the mitochondrial marker mitoBFP by four-color live-cell confocal microscopy. PDZD8 localized to ER membrane (Fig. 1D), which agrees with the results of a previous study (Hirabayashi et al., 2017). Remarkably, a fraction of PDZD8–GFP showed a ring pattern decorating the entire LE/lys membrane (Fig. 1D,E), and targeting of PDZD8 to LE/lys was accompanied by ER recruitment, as revealed by colocalization among ER-tagRFP, PDZD8–GFP and Lamp1–Halo and corresponding linescan analysis (Fig. 1E, row 1), indicating that PDZD8 was enriched at ER-LE/lys MCSs. PDZD8 was not specifically accumulated at ER–mitochondria MCSs, as shown by linescan analysis along ER tubules (Fig. 1E, row 2). Consistent with results from a recent study (Elbaz-Alon et al., 2020), we noted that PDZD8–GFP-decorated LE/lys appear to be in close proximity to mitochondria (Fig. 1E, rows 1 and 2).

To further validate the localization of PDZD8 at ER–LE/lys MCSs, we tracked the dynamics of PDZD8 relative to ER–LE/lys MCSs in the sPDZD8-GFP stable line transiently labeled with LE/lys and ER markers by live-cell confocal microscopy (Fig. 1F). PDZD8 was gradually recruited to ER–LE/lys MCSs as such contacts expanded and the level of PDZD8 was proportional to the extent of ER–LE/lys tethering (Fig. 1F; Movie 1), suggesting that PDZD8 is a tether between ER and LE/lys at the MCSs.

We further examined the localization of PDZD8 relative to LE/lys, ER and mitochondria by Lattice-SIM super-resolution microscopy. Compared to non-PDZD8-decorated LE/lys (Fig. 1G, white arrow), PDZD8-decorated LE/lys were completely wrapped around by ER tubules (Fig. 1G, yellow arrow).

We also tested whether PDZD8 was accumulated at ER–plasma membrane (PM) MCSs by live-cell confocal microscopy in sPDZD8–GFP cells (Fig. S2A,B) or HeLa cells transiently transfected with PDZD8–GFP (Fig. S2C,D). PDZD8 was not specifically colocalized with GFP-Mapper puncta, a known marker of ER–PM MCSs (Chang et al., 2013) in both cell lines examined, indicating that PDZD8 does not have a role in ER–PM MCSs.

The TM domain of PDZD8 anchors the ER while the C1-CC region targets LE/lys

The function of PDZD8 in tethering the ER to LE/lys requires the presence of binding sites responsible for recognizing these two membranes. Based on bioinformatics analysis, the domain organization of PDZD8 consists of an N-terminal TM domain, a SMP domain, a PDZ domain and a C1 domain, followed by a coiled-coil (CC) domain at its C terminus (Fig. 2A; Fig. S3A) (Fidler et al., 2016). In addition, the PDZ domain in human PDZD8 is inserted into the C2 domain, and therefore the C2 domain sequence in PDZD8 is split with ∼65 amino acids lying between the SMP and PDZ domains (residues 320–372), then the rest (residues 695–800) being before the C1 domain (Guillén-Samander et al., 2019; Wong et al., 2017). PDZD8 has been suggested to be an ER-resident protein with its N-terminal TM domain anchoring into ER membrane (Hirabayashi et al., 2017). Consistent with this finding, PDZD8 with a TM deletion (PDZD8-ΔTM) was cytosolic and failed to target the ER membrane, whereas a fraction of PDZD8-ΔTM was able to recognize LE/lys, as revealed by decoration of PDZD8-ΔTM on the entire LE/lys surface (Fig. 2B). Truncated PDZD8 containing the TM and SMP domains only (PDZD8-TM-SMP) displayed the same distribution as the full-length protein on ER membrane but without LE/lys localization (Fig. 2C). In addition, the SMP domain alone was cytosolic and failed to recognize either the ER or LE/lys membranes (Fig. S3B). Taken together, our results indicate that the N-terminal TM domain of PDZD8 is responsible for ER targeting, which is in agreement with recent studies (Elbaz-Alon et al., 2020; Guillén-Samander et al., 2019; Shirane et al., 2020).

Next, we dissected PDZD8 to identify the domains that were required for recognizing LE/lys by live-cell confocal microscopy in

Journal of Cell Science (2022) 135, jcs255026. doi:10.1242/jcs.255026

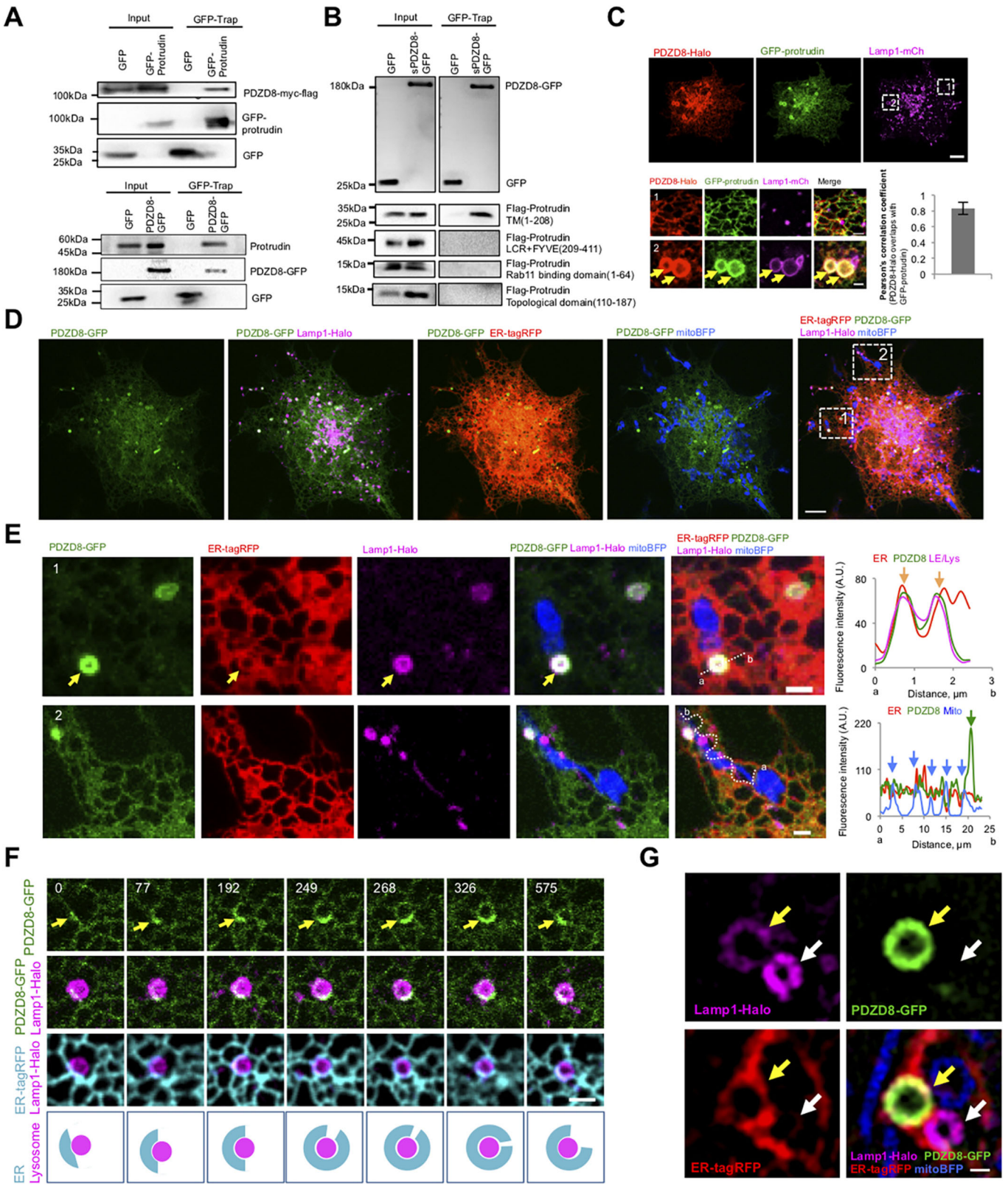

Fig. 1. See next page for legend.

COS7 cells transiently transfected truncated PDZD8 constructs (Fig. S3A) and LE/lys markers. Consistent with results from recent studies (Elbaz-Alon et al., 2020; Guillén-Samander et al., 2019; Shirane et al., 2020), we found that both the C-terminal C1 domain and the CC domain were required for targeting LE/lys membranes (Fig. 2D; Fig. S3C,D), as neither the C1 domain (Fig. 2E) nor the CC domain alone (Fig. 2F) was sufficient to recognize LE/lys membranes. In addition, neither PDZD8 without both the TM domain and C1-CC

Journal of Cell Science

Journal of Cell Science (2022) 135, jcs255026. doi:10.1242/jcs.255026

Fig. 1. PDZD8 localizes to ER–LE/lys MCSs. (A) Top, GFP-Trap assays were performed in COS7 cells expressing GFP–protrudin and PDZD8–Myc–Flag. Immunoblotting with antibodies against Flag and GFP was performed. Bottom, a GFP-Trap assay was performed in COS7 cells expressing PDZD8–GFP. Immunoblotting with antibodies against protrudin and GFP was performed. GFP empty vector was used as control. (B) GFP-Trap assays were performed in COS7 cells expressing PDZD8–GFP and Flag-tagged protrudin fragments. Immunoblotting with antibodies against Flag and GFP was performed. GFP empty vector was used as control. (C) Representative confocal image of a live COS7 cell expressing PDZD8–Halo, GFP–protrudin and Lamp1–mCherry. Top panel, images of the whole cell. Bottom panel, magnified views of area indicated by boxes (labeled 1 and 2). Yellow arrows denote PDZD8 and protrudin colocalization at ER-LE/lys MCSs with Pearson's correlation coefficient analysis of PDZD8–Halo and GFP–protrudin shown in the graph [mean±s.d. (n=57 cells)]. (D) Representative confocal images of a live COS-7 cell stably expressing EF1α promoter-driven PDZD8–GFP (green) and transiently transfected with Lamp1–Halo, ER-tagRFP and mitoBFP. (E) Two areas from D were shown at enlarged sizes with linescans of the dotted line on the right. Yellow arrows denote the enrichment of PDZD8–GFP at ER–LE/lys MCSs. (F) Time-lapse images of a COS7 cell as in D showing PDZD8–GFP (green) specifically enriched at ER (cyan)–LE/lys (magenta) MCSs over time (given in seconds). Yellow arrows denote the gradual accumulation of PDZD8–GFP as the ER–LE/lys MCSs expands. (G) Representative Lattice-SIM images of a live COS7 as in D showing a PDZD8 (green)-decorated LE/lys (magenta) wrapped around by ER tubules (red). Yellow arrows denote PDZD8-decorated LE/lys wrapped by ER, whereas white arrows indicate a non-PDZD8 decorated LE/lys without ER wrapping. Scale bars: 10 µm (whole-cell image in C,D); 2 µm (enlarged images in C,E,F); 0.5 µm (G).

domain (PDZD8-ΔTM-ΔC1-ΔCC) (Fig. 2G) nor PDZD8 without the C1 and CC domain (PDZD8-ΔC1-ΔCC) (Fig. 2H) was able to target LE/lys. These findings indicate that the C1-CC domain is necessary and sufficient for PDZD8 to target LE/lys membranes (Fig. 2I). Besides COS7 cells, PDZD8-C1-CC was able to recognize LE/lys membranes in multiple animal cell lines, including HeLa, U2OS and Neuro-2a cell lines (Fig. S4), suggesting LE/lys recognition by PDZD8-C1-CC is conserved among cell types.

The C1-CC region of PDZD8 targets LE/lys through directly binding Rab7

We next sought to understand the molecular mechanisms underlying the recognition of LE/lys membrane by the C1-CC domain. Neither the C1 domain nor the CC domain is likely to directly bind to lipid bilayer of LE/lys membranes (Hurley and Misra, 2000; Truebestein and Leonard, 2016). Thus, we hypothesized that C1-CC domains may bind to proteins on LE/lys membrane to mediate LE/lys recognition. Using GFP-Trap followed by MS analysis, we identified PDZD8-interacting proteins in sPDZD8-GFP COS7 cells. We focused on proteins belonging to the following two categories. First, it was exclusively present in the list after removal of proteins coIPed by GFP alone; second, it was a LE/lys membrane protein. From the list of protein candidates selected based on the rules described above (Fig. S5A), we performed a brief screening by co-expressing identified protein candidates with PDZD8-C1-CC and examining whether the protein candidates could enhance the LE/lys recruitment of PDZD8-C1-CC by live-cell confocal microscopy in COS7 cells. Among seven candidates examined in the screening, only Rab7a expression substantially boosts the C1-CC recruitment to LE/lys membrane (Fig. 3A,E). We further tested the roles of two Rab7a mutants on C1-CC recruitment. Co-expression of Rab7a(Q67L), a constitutively active mutant, greatly enhances C1-CC recruitment to LE/lys (Fig. 3B,E), whereas Rab7a(T22N), a dominant-negative mutant, blocked C1-CC recruitment to LE/lys (Fig. 3C,E). In addition, PDZD8-C1-CC was not substantially recruited to Rab5-positive early endosomes even when Rab5a was co-expressed (Fig. 3D,E), indicating that the recruitment of C1-CC to LE/lys was Rab7 specific, which is consistent with results from recent studies (Elbaz-Alon et al., 2020; Guillén-Samander et al., 2019; Shirane et al., 2020).

Since PDZD8 interacted and colocalized with protrudin, there was a possibility that PDZD8-C1-CC recognized LE/lys membrane through protrudin. Suppression of protrudin did not substantially hamper PDZD8-C1-CC recruitment to LE/lys compared with the scrambled siRNA-treated cells (Fig. S5B,D,F,H), whereas suppression of Rab7 via Rab7a siRNA-mediated knockdown almost completely blocked PDZD8-C1-CC recruitment (Fig. S5B,C,F,I), ruling out the possibility that PDZD8-C1-CC recognizes LE/lys through protrudin. Suppression of VPS37B, an ESCRT-I component identified from PDZD8-GFP coIP-MS analysis did not substantially inhibit PDZD8-C1-CC recruitment (Fig. S5E,F). In addition, because protrudin is known to recognize LE/lys membrane in a bipartite manner through binding to Rab7 and PI3P (Raiborg et al., 2015a), we investigated whether PI3P was required for the recruitment of the PDZD8-C1-CC region to LE/lys membranes. Inhibition PI3P synthesis by wortmannin or VPS34IN1 treatment, failed to halt PDZD8-C1-CC recruitment to LE/lys in COS7 cells transiently transfected with PDZD8-C1-CC and Flag–Rab7, although LE/lys were enlarged and clustered near nucleus after these treatments (Fig. S5G).

We further investigated whether PDZD8-C1-CC directly binds to Rab7 *in vitro*. Glutathione S-transferase (GST) pulldown assays with purified proteins showed that GST-tagged C1-CC but not GST alone, interacted directly with GTP- (but not GDP-) loaded Rab7, and that there was no interactions with Rab5-GTP (Fig. 3F), consistent with results from a recent study (Guillén-Samander et al., 2019). Thus, PDZD8 is a new Rab7 effector that interacts with this protein through its C1-CC region. Taken together, these findings demonstrate that PDZD8-C1-CC recognizes LE/lys membrane through Rab7, in line with the recent studies (Elbaz-Alon et al., 2020; Guillén-Samander et al., 2019; Shirane et al., 2020).

Rab7 activities control PDZD8-mediated ER-LE/lys MCSs

The presence of Rab7 in PDZD8 mediated ER-LE/lys MCSs raised a question of whether the activity of Rab7 regulated PDZD8-mediated ER-LE/lys tethering. Coexpressing Rab7 or Rab7(Q67L) in the sPDZD8-GFP line resulted in specific and dramatic recruitment of full-length PDZD8 to entire surface membrane of LE/lys, indicating that LE/lys were entirely wrapped by ER tubules, whereas PDZD8 only decorated a few LE/lys membrane in control sPDZD8-GFP cells transiently transfected with the LE/lys marker Lamp1 (Fig. 4A–C). Conversely, coexpressing Rab7(T22N) completely blocked the recruitment of full-length PDZD8 to LE/lys membrane (Fig. 4D), indicating that Rab7 activity controlled PDZD8-mediated ER–LE/lys MCSs. Notably, upon overexpression of either Rab7 wild-type (WT) or Rab7(Q67L), PDZD8 was strongly recruited to ER–LE/lys MCSs so that ER-localized, non-MCS PDZD8 was hardly detectable, while the amount of PDZD8-decorated LE/lys was much less; ER-resident, non-MCS PDZD8 signals were readily detectable in neighboring non-Rab7-transfected cells (Fig. 4B,C). In contrast, overexpression of Rab7(T22N) completely blocked recruitment of PDZD8 to LE/lys and ER-resident, non-MCS PDZD8 was easily detectable (Fig. 4D), suggesting that Rab7 recruits PDZD8 from ER pools to LE/lys membranes to mediate ER–LE/lys tethering.

To further validate the tethering functions of PDZD8, we examined the level of the ER–LE/lys interactions by live-cell confocal microscopy in COS7 cells. Compared to cells only

Journal of Cell Science (2022) 135, jcs255026. doi:10.1242/jcs.255026

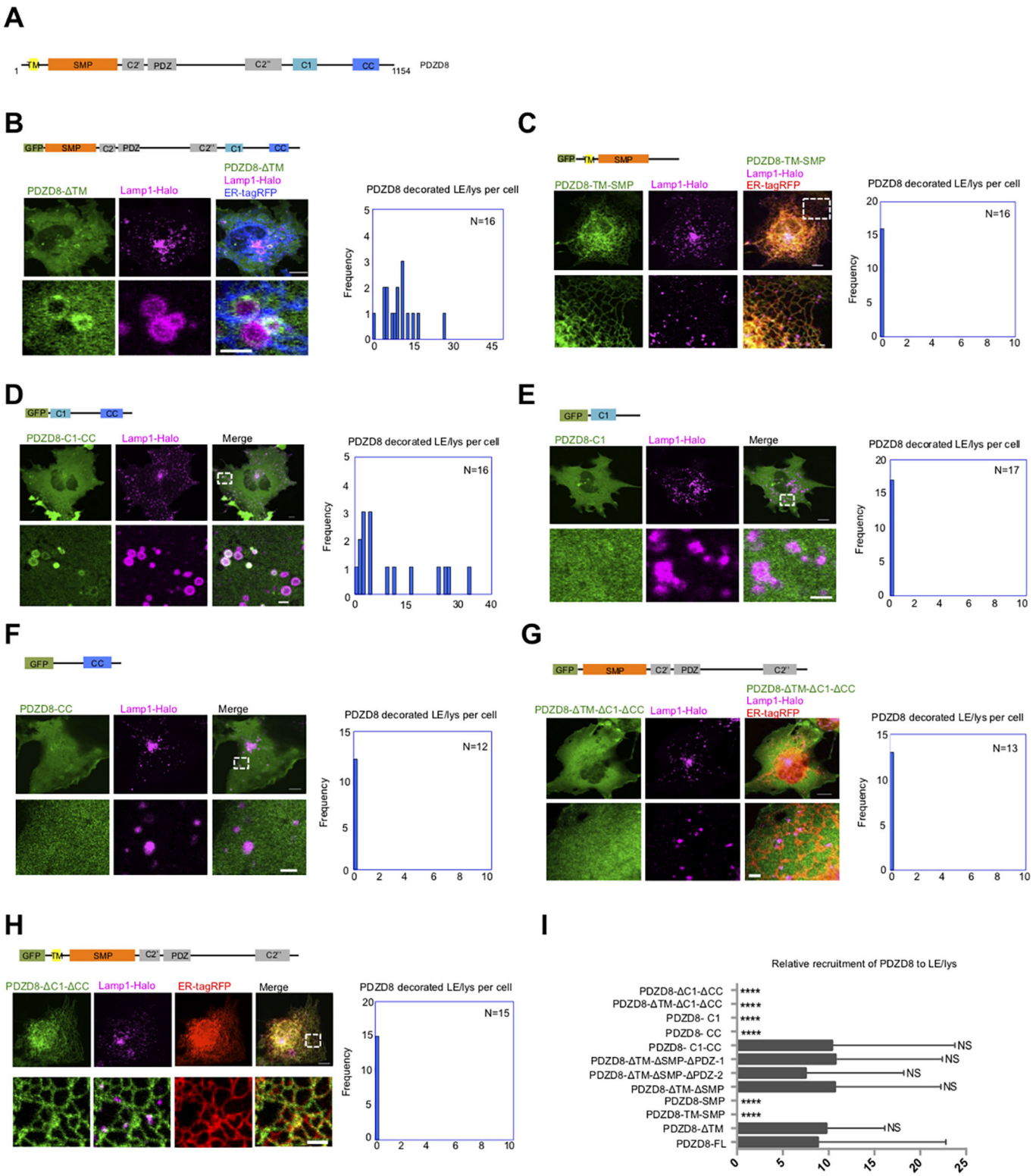

Fig. 2. The N-terminal TM domain and the C-terminal C1-CC region is responsible for PDZD8 localization to ER–LE/lys MCSs. (A) Diagram demonstrating PDZD8 domains. (B–H) Representative confocal images of COS7 cells transiently expressing truncated PDZD8 (green) relative to LE/lys (magenta) or ER (red) with whole-cell images in the top row and enlarged views of the boxed area on the bottom row. The quantification of frequency of truncated PDZD8 coating LE/lys is shown on the right. N represented cell number in the analysis. (I) Quantification of number of full-length PDZD8 or truncated PDZD8 mutation decorated LE/lys. Full-length PDZD8 (n=52); PDZD8-ΔTM (n=16); PDZD8-TM-SMP (n=16); PDZD8-SMP (n=16); PDZD8-ΔTM-ΔSMP (n=16); PDZD8-ΔTM-ΔSMP-ΔPDZ-2 (n=12); PDZD8-ΔTM-ΔSMP-ΔPDZ-1 (n=16); PDZD8-C1-CC (n=16); PDZD8-CC (n=16); PDZD8-C1 (n=16); PDZD8-ΔTM-ΔC1-ΔCC (n=16); PDZD8-ΔC1-ΔCC (n=16). ****P<0.0001; NS, not significant (P>0.05) (two-tailed unpaired Student's t-test). Mean±s.d. Scale bars: 10 µm (whole-cell image in B–H); 2 µm (enlarged images in B–H).

Journal of Cell Science (2022) 135, jcs255026. doi:10.1242/jcs.255026

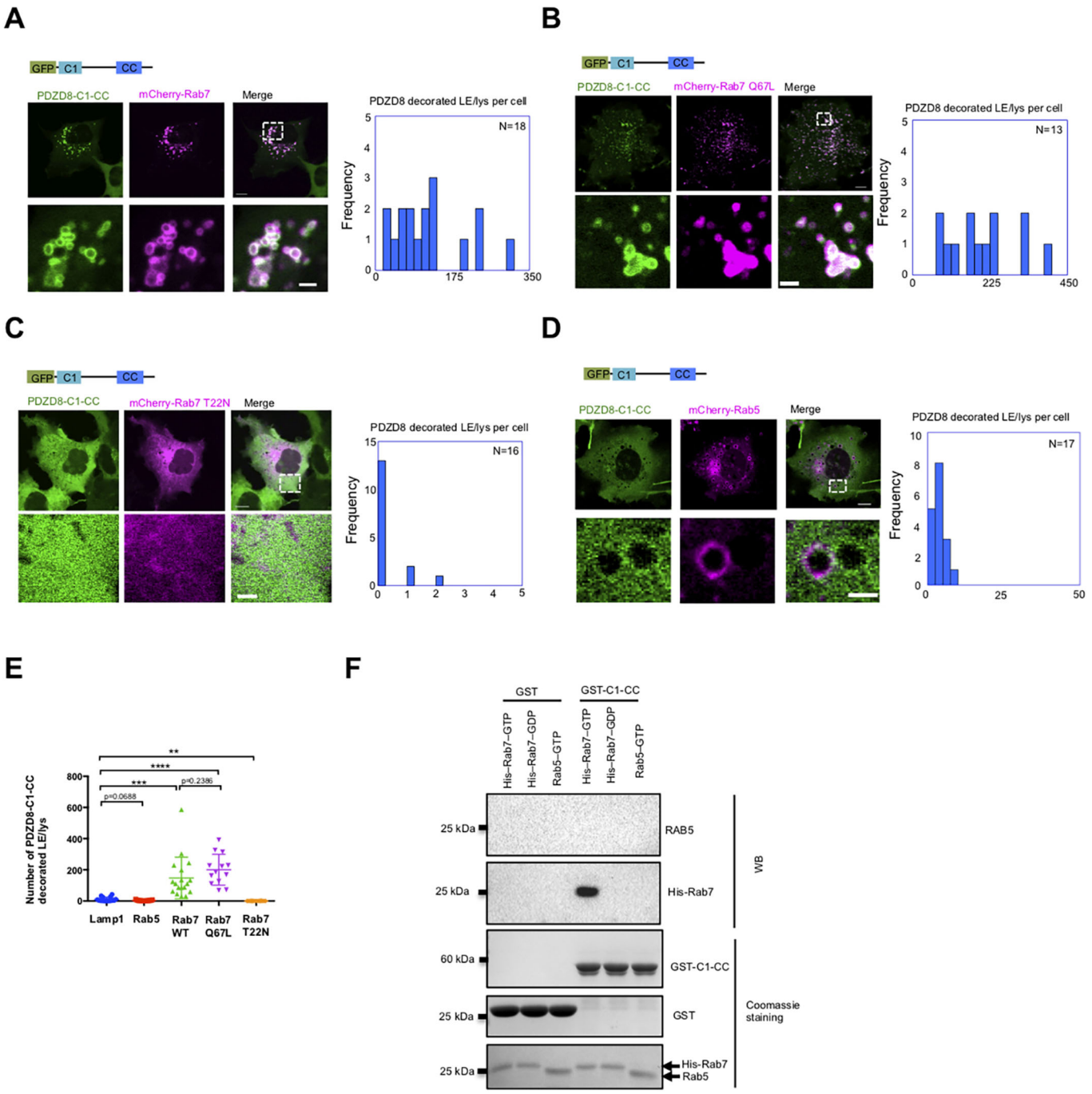

Fig. 3. The C1-CC region of PDZD8 recognizes LE/lys by directly binding Rab7. (A–D) Representative confocal images of a COS7 cell transiently expressing GFP–C1-CC (green) and mCherry–Rab7 (A, magenta), mCherry-Rab7(Q67L) (B, magenta), mCherry–Rab7(T22N) (C, magenta) or mCherry–Rab5 (D, magenta) with whole cell image on top and insets on bottom. Quantification of frequency of PDZD8-C1-CC decorated LE/lys is shown on the right. N represents cell number in the analysis. (E) Quantification of the number of PDZD8-C1-CC decorated LE/lys. Lamp1 (n=16); Rab5 (n=17); Rab7 (n=18); Rab7 Q67L (n=13); Rab7 T22N (n=16); ****P<0.0001; ***P=0.0003; **P=0.0052; not significant are those over P>0.05 (two-tailed unpaired Student's t-test). Mean±s.d. (F) GST pulldown assay of purified GST–C1-CC interacting with His–Rab7 or Rab5 *in vitro*. Western blots using anti-Rab5 antibody and anti-His antibody are shown in the upper panel. The Coomassie Blue staining of purified GST–C1-CC (top), GST (middle), and His–Rab7 and Rab5 (bottom) used in the pulldown reactions is shown in the bottom panel. Images representative of three independent experiments. Scale bars: 10 µm (whole-cell images in A–D); 2 µm (enlarged images in A–D).

transfected with the LE/lys marker Lamp1–mCherry and the ER marker GFP–Sec61β, co-overexpression of Rab7 and PDZD8 substantially enhanced the extent of ER–LE/lys interactions, as revealed by the colocalized pixels between these two organelles, whereas overexpression of Rab7 alone could only slightly increase ER–LE/lys interactions (Fig. 4E–H), indicating that both PDZD8 and Rab7 are required and sufficient for ER–LE/lys tethering, which confirms the key findings in recent results (Elbaz-Alon et al., 2020; Guillén-Samander et al., 2019; Shirane et al., 2020).

PDZD8–Rab7-mediated ER-LE/lys tethering was further examined by four-color live-cell super-resolution lattice-SIM microscopy in the sPDZD8-GFP stable line transiently expressing Flag–Rab7 along with ER, mitochondria and LE/lys markers.

Journal of Cell Science (2022) 135, jcs255026. doi:10.1242/jcs.255026

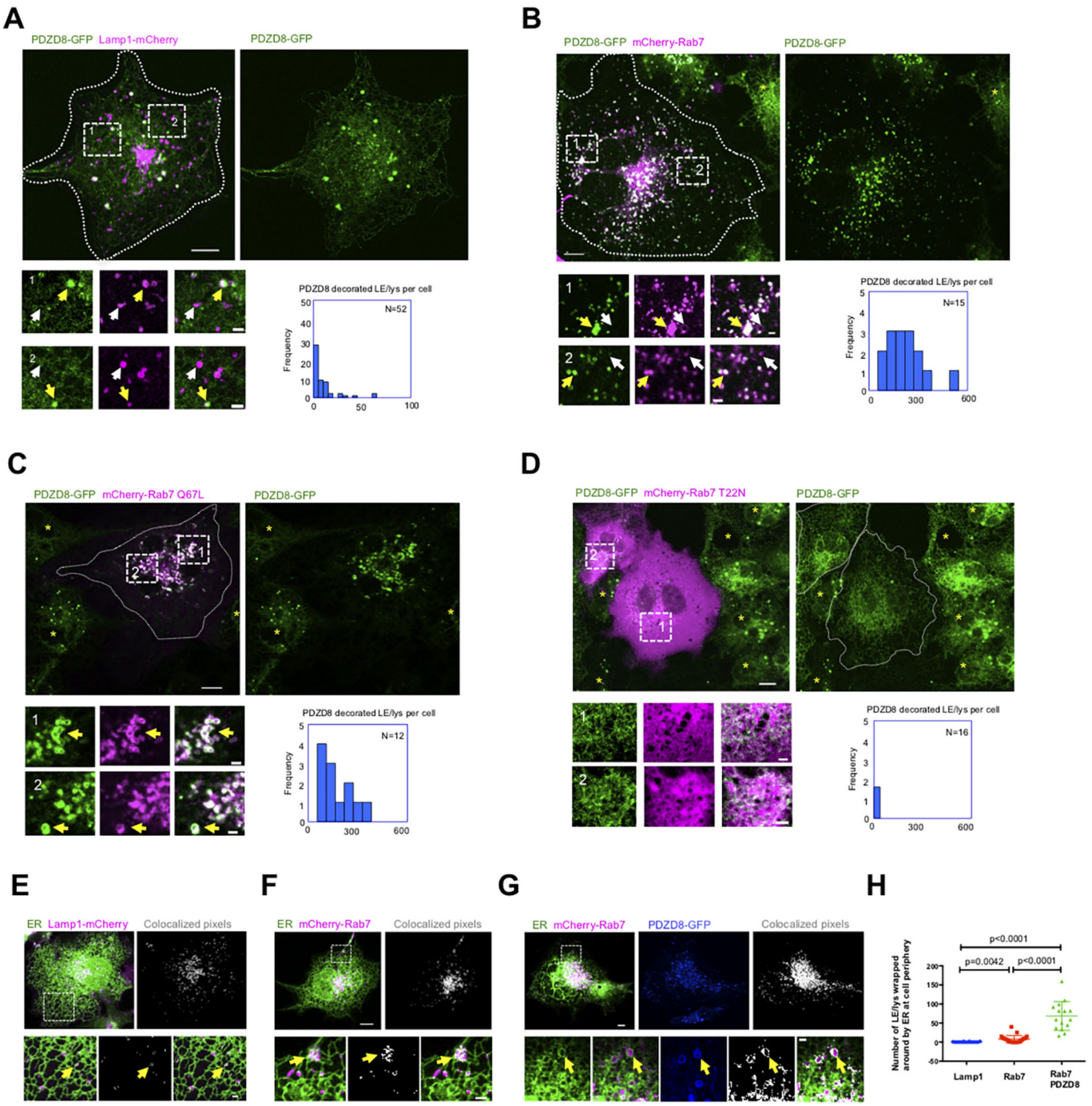

Fig. 4. Rab7 regulated the formation of PDZD8-mediated ER-LE/lys MCSs. (A–D) Representative confocal images of live sPDZD8-GFP (green) COS7 cells expressing with Lamp1–mCherry (A, magenta), mCherry–Rab7 (B, magenta), mCherry–Rab7(Q67L) (C, magenta) or mCherry–Rab7(T22N) (D, magenta). Left top panel, merged images of whole cell; right top panel, PDZD8-GFP-only (green); bottom panels, magnified images from boxed regions in whole-cell image. Yellow arrows indicate PDZD8-decorated LE/lys; white arrows indicate LE/lys without PDZD8 decoration. Quantification of frequency of PDZD8 decorated LE/lys was shown on the right of magnified images. N represents cell number in the analysis. (E–G) Representative confocal images of live COS7 cells expressing ER–Halo (green) and Lamp1–mCherry (E, magenta), mCherry–Rab7 (F, magenta) or co-expression of mCherry–Rab7 and PDZD8–GFP (G, magenta). Left top panel, merged image of whole cell; right top panel, colocalized pixels between ER and LE/lys (white); bottom panels, magnified images from boxed region in whole-cell image. (H) Quantification of number of LE/lys wrapped around by ER at cell periphery. Lamp1 (n=16); Rab7 (n=23); Rab7 and PDZD8 (n=15). P-values are as shown (two-tailed unpaired Student's t-test). Mean±s.d. Scale bars: 10 µm (whole-cell images in A–G); 2 µm (enlarged images in A–G).

Co-expression of Rab7 and full-length PDZD8 caused an extensive ER–LE/lys tethering, as revealed by ER tubules completely (Fig. 5A–C, box 2 images) or partially (Fig. 5A–C, boxes 3–7) wrapping the LE/lys with specific enrichments of PDZD8 at such contacts (Fig. 5A–C).

The SMP domain of PDZD8 binds glycerophospholipids and ceramide both *in vitro* and *in vivo*, and mediates lipids transport *in vitro*

The localization of PDZD8 at ER–LE/lys MCSs is consistent with a potential role of SMP domain-containing proteins in lipid transport

Journal of Cell Science (2022) 135, jcs255026. doi:10.1242/jcs.255026

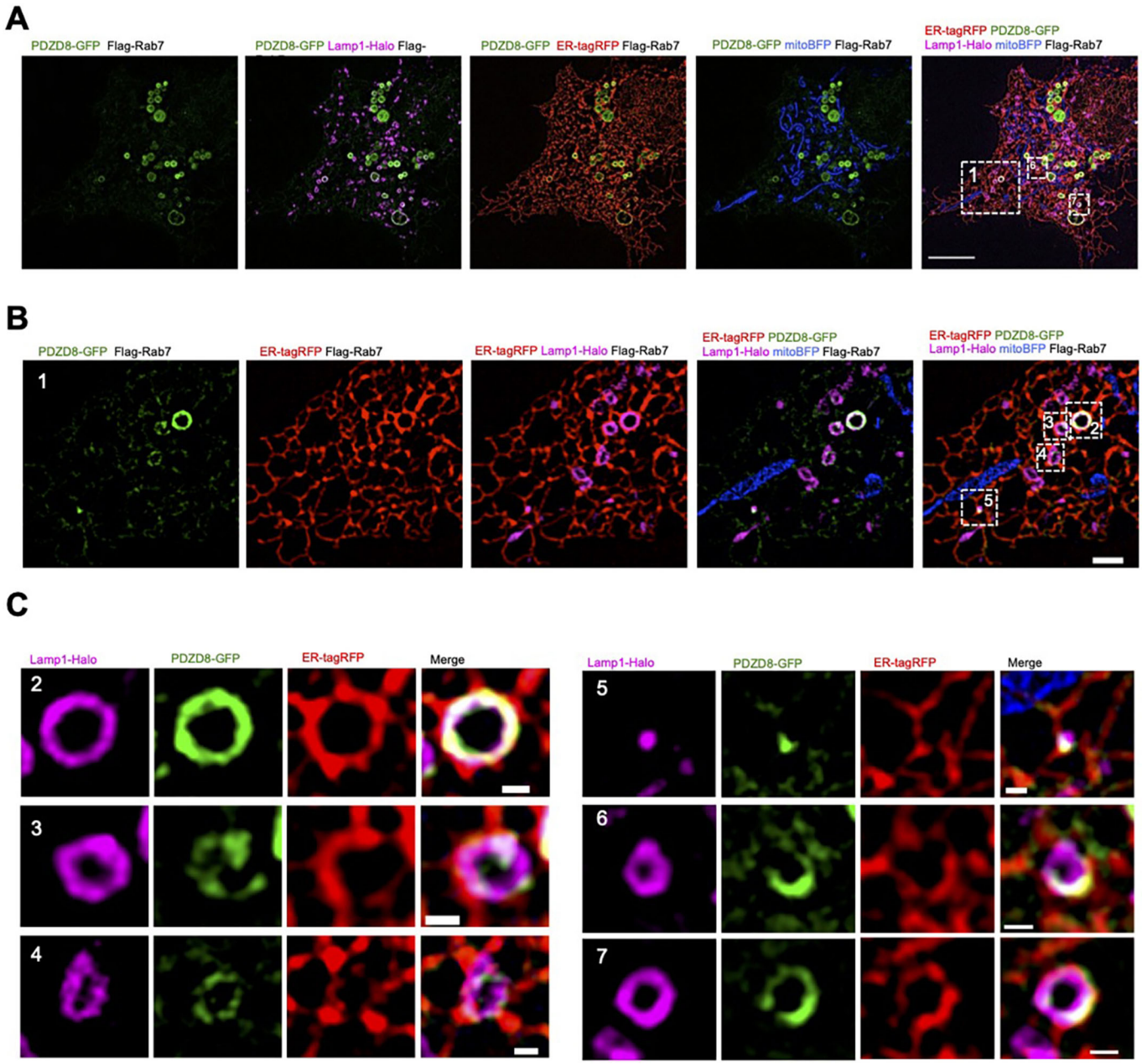

Fig. 5. Lattice-SIM images of PDZD8–Rab7-mediated ER-LE/lys MCSs. (A) Super-resolution lattice-SIM whole-cell images of a live iRab7-sPDZD8-GFP cell expressing Lamp1–Halo, ER-tagRFP, and mitoBFP along with Dox-inducible expression of Flag-Rab7. (B) Enlarged views from area indicated by the box 1 in the whole image in A. (C) Six more enlarged views (boxed areas denoted by numbers) from A and B showing ER-LE/lys MCSs with specific enrichment of PDZD8. Scale bars: 10 µm (whole cell image in A); 2 µm (B); 0.5 µm (C).

between adjacent organelles. Therefore, we next tested the possibility that PDZD8 might directly bind and transport lipids. To investigate whether PDZD8 might solubilize lipids, a prerequisite for a lipid transport function, we examined lipid species bound by full-length PDZD8 in sPDZD8-GFP COS7 cells infected with a doxycycline-inducible lentiviral vector encoding Flag–Rab7 (Fig. S6A). Our rationale of using inducible expression of Rab7 in sPDZD8-GFP cells (iRab7-sPDZD8-GFP) for this assay was that PDZD8 presumably binds lipids at ER–LE/lys MCSs and inducible expression of Rab7 would enable a transient increase in PDZD8-mediated contacts. Lipid species associating with PDZD8–GFP were assessed by non-targeted lipidomics using liquid chromatography-tandem mass spectrometry (LC-MS/MS) with rigorous washes of the protein before lipid analysis. PDZD8–GFP mainly associated with glycerophospholipids [lysophosphatidylcholines and phosphatidylcholines (LPC/PC), phosphatidylserine (PS) and phosphatidic acid (PA)], and a few ceramides and sphingomyelin (SM) but no sterols were detected using GFP tag-only as a control (Fig. 6A). Since PDZD8 harbors two potential lipid-binding domains (SMP and C1), we next assessed lipids bound by the SMP domain or the C1 domain alone by LC-MS/MS. We found that both the species and abundance of lipids co-purified with SMP–GFP highly resembled those of lipids co-purified with full-length PDZD8–GFP (Fig. 6A,B). We could not obtain significant results from the C1 domain using LC-MS/MS comparing with GFP tag control (data not shown). Therefore, this line of evidence indicates

Journal of Cell Science (2022) 135, jcs255026. doi:10.1242/jcs.255026

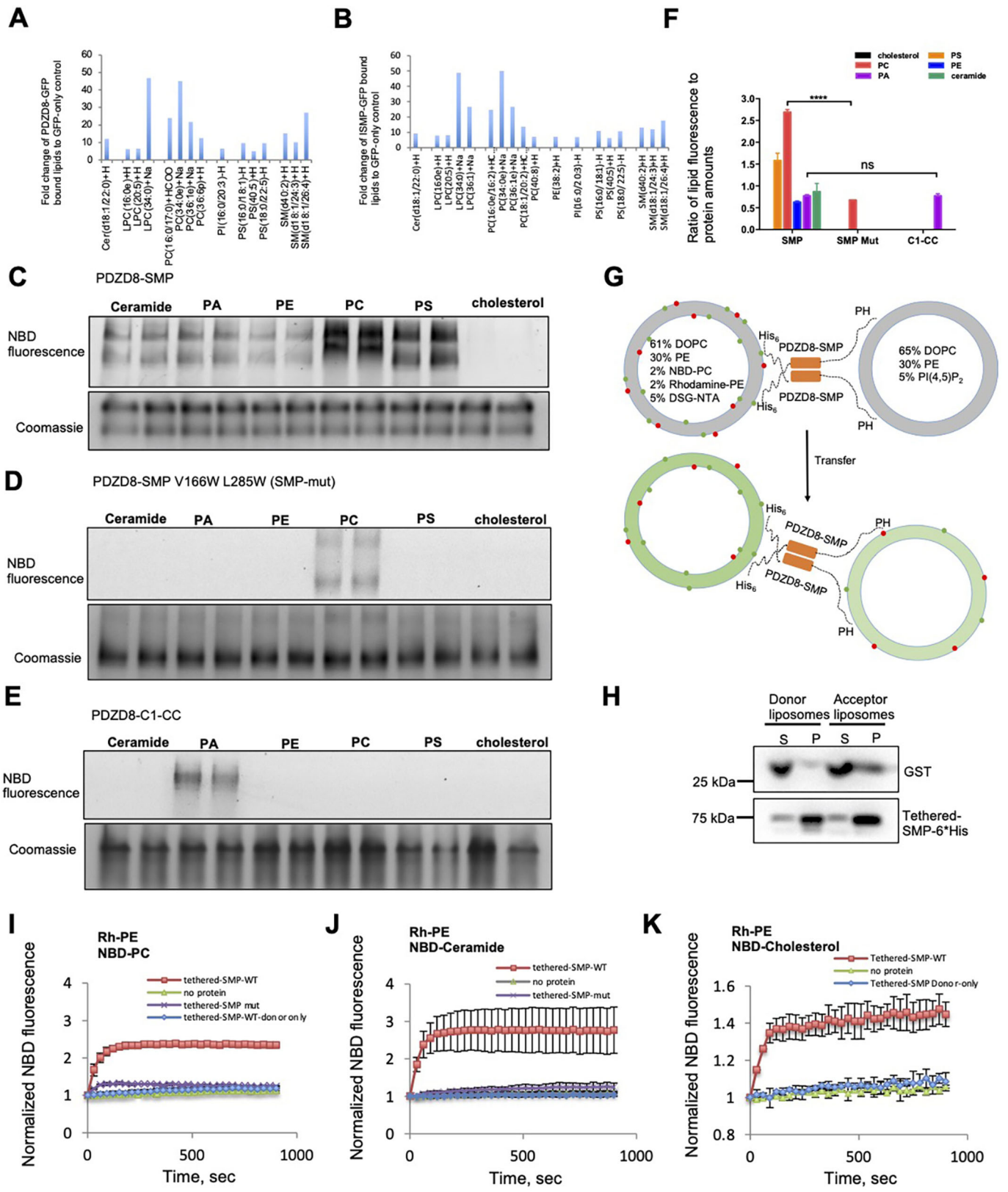

Fig. 6. See next page for legend.

that PDZD8 solubilized glycerophospholipids and ceramides through the SMP domain. In addition, we calculated the ratio of the specific lipids bound by PDZD8–GFP (Fig. S6B, left panel) or SMP–GFP (Fig. S6B, right panel) to the total amounts of the specific lipids extracted from COS7 cells. We found that both the PDZD8 and the SMP domain bound a very small amount of lipids

Journal of Cell Science (2022) 135, jcs255026. doi:10.1242/jcs.255026

Fig. 6. The SMP domain of PDZD8 binds glycerophospholipids and ceramides *in vivo* and *in vitro* and mediates lipid transfer *in vitro*. (A,B) Fold change of lipids that were associated with PDZD8–GFP (A) or SMP–GFP (B) compared to GFP control in Rab7-inducible COS7 cells. (C–E) *In vitro* lipid-binding assays for the SMP domain of PDZD8 (C), the SMP mutant V166W L285W (D) or the C1-CC region of PDZD8 (E). (F) Fold change of lipid fluorescence to protein levels for experiments in C–E. Three repeated experiments were analyzed. ****P<0.0001; ns, not significant (two-tail unpaired Student's *t*-test). Mean±s.d. (G) Schematic representation of the FRET-based *in vitro* lipid transfer assay of the tethered SMP domain of PDZD8. (H) Liposome pulldown assay confirmed the efficient binding of tethered SMP to both donor liposomes and acceptor liposomes. GST proteins were used as a negative control. Western blots were performed with antibodies against GST and His. S, supernatant; P, pellet. (I) Donor liposomes (20 µM) containing fluorescent lipids (2% NBD-PC, 2% Rhodamine-PE, 5% DGS-NTA, 61% DOPC, and 30% PE) were mixed 1:1 with acceptor liposomes [25 µM: 65% DOPC, 30% PE, and 5% $PI(4,5)P_2$] in the absence or presence of tethered PDZD8-SMP proteins (2 µg), or PDZD8-SMP-mut (2 µg). The NBD fluorescence was normalized to the fluorescence intensity at time=0. Mean±s.d. (J) As in I, donor liposomes (20 µM) containing fluorescent lipids (2% NBD-ceramide, 2% Rhodamine-PE, 5% DGS-NTA, 61% DOPC, and 30% PE) were mixed 1:1 with acceptor liposomes [25 µM: 65% DOPC, 30% PE, and 5% $PI(4,5)P_2$] in the absence or presence of tethered PDZD8-SMP proteins (2 µg) or PDZD8-SMP-mut (2 µg). The NBD fluorescence was normalized to the fluorescence intensity at time=0. Mean±s.d. (K) As in I, donor liposomes (20 µM) containing fluorescent lipids (2% NBD-cholesterol, 2% Rhodamine-PE, 5% DGS-NTA, 61% DOPC, and 30% PE) were mixed 1:1 with acceptor liposomes [25 µM: 65% DOPC, 30% PE, and 5% $PI(4,5)P_2$] in the absence or presence of tethered PDZD8-SMP proteins (2 µg). The NBD fluorescence was normalized to the fluorescence intensity at time=0. Mean±s.d.

[for example, only ∼5.8% of total ceramide (d18:1/22:0) content of cellular membranes was bound by PDZD8-GFP; and ∼4.5% of this lipid species bound by SMP–GFP] *in vivo*.

We further explored lipid-binding activities of PDZD8 by *in vitro* lipids-binding assays. So far, we cannot produce full-length proteins in sufficient quantities for biochemical analysis. Thus, we used purified PDZD8 fragments for this purpose. Consistent with our LC-MS/MS results, the SMP domain of PDZD8 co-migrated with nitrobenzoxadiazole (NBD)-labeled glycerophospholipids [PS, PC, phosphatidylethanolamine (PE) and PA] and ceramides but not cholesterols, as assessed by native gel electrophoreses (Fig. 6C). Among these lipids, the SMP domain preferentially bound to PC and PS (Fig. 6C,F). We made a space-filling SMP mutant of PDZD8 (SMP-mut), in which two residues with small hydrophobic side-chains were replaced with tryptophan residues, which have with large side-chains (V166W, L285W), according to an approach previously reported in an elegant study (Saheki et al., 2016) (Fig. S6C). We found that the purified SMP-mut did not bind to these lipids except for a low binding affinity to PC (Fig. 6D,F). We also assessed the lipid-binding activities of the C1-CC region via *in vitro* lipid-binding assays. C1-CC barely bound NBD-labeled PC, PS, PE and ceramides, but bound NBD-PA at a low level (Fig. 6E,F), consistent with our LC-MS/MS results and indicating that the SMP domain is responsible for the lipid-binding activities of PDZD8.

Based on these observations, we next employed a fluorescence resonance energy transfer (FRET)-based assay to examine whether the SMP domain transported lipids between membranes according to the strategy developed by previous studies (Kumar et al., 2018; Saheki et al., 2016; Valverde et al., 2019; Yu et al., 2016). Briefly, donor liposomes containing DGS-NTA, NBD-PC and Rhodamine-PE (Rh-PE) were mixed with non-fluorescent acceptor liposomes containing phosphatidylinositol 4,5-bisphosphate [$PI(4,5)P_2$], and then purified 'tethered SMP domain' proteins were added. This tethered SMP domain is tethered to donor liposomes via a N-terminal hexahistidine (His) tag and is also tethered to acceptor liposomes through a C-terminal pleckstrin homology (PH) domain, which interacts with $PI(4,5)P_2$ in the acceptor liposomes. Thus, the linker tethered together donor and acceptor liposomes to mimic the architecture of MCSs, where the PDZD8-SMP likely functions (Fig. 6G).

To confirm that the tethered SMP domain was able to bind donor and acceptor liposomes, we conducted liposome pulldown assays. We found that the tethered SMP domain, but not GST, could efficiently bind both the donor and acceptor liposomes (Fig. 6H). In addition, we further examined the liposome tethering efficiency by measuring the size distribution of liposomes, in the presence or absence of the tethered SMP domain, via dynamic light scattering (DLS). The DLS assays indicated that the addition of tethered SMP (but not the no-protein control or the addition of GST) resulted in a substantial increase in size of liposomes (Fig. S6D), indicating that the tethered SMP efficiently bridges donor and acceptor liposomes. We also observed that the addition of tethered SMP resulted in two peaks, with a smaller one at ∼400 nm (this might suggest about four liposomes cross-linked) and a larger one at ∼5000–6000 nm (tens of liposomes cross-linked) (Fig. S6D). In addition, the DLS assays indicate that the liposomes in absence of tethered SMP are well dispersed, uniform in size (∼100 nm) and stable in solution, suggesting no spontaneous fusion or hemifusion of liposomes without tethered SMP proteins.

Initially, FRET between NBD and Rh in the donor liposomes quenched NBD fluorescence. Transfer of NBD-PC, Rh-PE or both to acceptor liposomes would result in their dilution, decreased FRET and thus an increase in NBD fluorescence. We observed an increase in NBD fluorescence upon addition of the wild-type (WT) tethered SMP (but not the no-protein control; Fig. 6I). We investigated the lipid transfer activities of the space-filling mutant SMP-mut using *in vitro* lipid transfer assays. Consistent with our *in vitro* lipid-binding assays, in which the SMP-mut still binds to PC in a low level (Fig. 6D), SMP-mut caused a substantial decrease in the transfer of NBD-PC or Rh-PE comparted to the non-mutant form, but did not completely lose the transfer activities, as revealed by a very small increase in NBD fluorescence in presence of donor liposomes containing NBD-PC, Rh-PE and non-fluorescent acceptor liposomes (Fig. 6I, purple curve). In contrast to a robust increase in NBD fluorescence upon the addition of the WT tethered SMP, the addition of SMP-mut failed to increase NBD fluorescence in presence of donor liposomes containing NBD-ceramide, Rh-PE and acceptor liposomes (Fig. 6J, purple curve), which agrees with our *in vitro* lipid-binding assay, in which the SMP-mut did not bind either ceramide or PE. This result suggests that PDZD8-SMP is able to transfer PC, PE and ceramides *in vitro*. However, it should be noted that the FRET-based assays do not discriminate whether the PDZD8-SMP transports PE only, PC only, ceramide only, or the three lipids. We therefore examined whether PDZD8-SMP transported PE using *in vitro* lipid transfer assays with donor liposomes containing NBD-cholesterol and Rh-PE, and acceptor liposomes. Owing to the lack of suitable commercial Rhodamine-labeled lipids (such as Rh-cholesterol, Rh-PC or Rh-ceramide), in this study we only investigated the PE transfer activity of the SMP domain *in vitro*. We observed an increase in NBD fluorescence upon addition of the tethered SMP-WT (but not the no-protein control; Fig. 6K). Since our results indicate that the PDZD8-SMP does not bind NBD-cholesterol (Fig. 6C), the increase in NBD fluorescence indicated the transfer of Rh-PE from donor liposomes to acceptor liposomes mediated by PDZD8-SMP.

In addition, the NBD fluorescence of reactions with or without tethered SMP was almost the same following the further addition of

Journal of Cell Science (2022) 135, jcs255026. doi:10.1242/jcs.255026

dithionite (Meers et al., 2000), which quenches NBD fluorescence only in the outer leaflet of the liposome bilayer but does not affect the inner leaflet, ruling out the possibility that the tethered SMP-mediated fluorescence increase is due to fusion or hemifusion between donor and acceptor liposomes (Fig. S6E).

Notably, we observed that there was no substantial increase in NBD fluorescence in reactions with the tethered SMP and donor liposomes lacking acceptor liposomes (Fig. 6I–K), corresponding to a scenario in which PDZD8-SMP extracts fluorescent lipids from the donor liposomes, but cannot deliver them to acceptor liposomes. This result indicates that the SMP domain of PDZD8 extracted only a small amount of lipids from acceptor liposomes, and therefore the dilution of NBD-PC and Rh-PE was not strong enough to activate NBD fluorescence. Our results were in accordance with the SMP module of the previously characterized glycerophospholipid transporter extended synaptotagmin 1 (E-Syt1), in which the lipid-extracting activities of E-Syt1 was also very low in similar reactions with purified E-Syt1 and donor liposomes but without acceptor liposomes (Kumar et al., 2018; Saheki et al., 2016; Valverde et al., 2019; Yu et al., 2016). This line of evidence supports that PDZD8-SMP might act as a shuttle transporter that extracts and solubilizes lipids (one or two lipid molecules at once) from the membrane of the donating organelle, ferries them through the cytosol, and then deposits them in the membrane of the acceptor organelle (Li et al., 2020; Wong et al., 2017).

Moreover, since SMP domain-containing proteins such as E-Syts form dimers through SMP domain dimerization (Reinisch and De Camilli, 2016), we tested whether PDZD8 also formed dimers or oligomers. We first examined the oligomeric status of PDZD8 by GFP-Trap assays in sPDZD8-GFP cells transiently transfected with PDZD8–Myc–Flag. The GFP-trap assay showed that PDZD8–Myc–Flag was co-pelleted with PDZD8–GFP (Fig. S6F). In addition, PDZD8-TM-SMP sufficiently co-pelleted with full-length PDZD8–Myc–Flag, whereas PDZD8 lacking the SMP domain could not bind PDZD8–Myc–Flag, indicating that PDZD8 formed dimers or oligomers through the SMP domain (Fig. S6F). Moreover, the level of PDZD8–Myc–Flag co-pelleted by TM-SMP was less than that of full-length PDZD8, suggesting that other regions may also contribute or stabilize the oligomerization of PDZD8 (Fig. S6F). Notably, TM-SMP tended to be dimerized even in denatured conditions, as revealed by two bands in western blots, one band with a molecular mass of ∼75 kDa, the other of ∼150 kDa, were present in both input and GFP-trapped samples (Fig. S6F, red asterisks). In addition, we found that PDZD8 lacking C1-CC (PDZD8-ΔC1-ΔCC) could interact with protrudin, and the C1-CC regions may contribute to PDZD8–protrudin interactions because the level of protrudin co-pelleted by PDZD8-ΔC1-ΔCC was less compared to level of protrudin co-pelleted by full-length PDZD8 (Fig. S6F).

Lipid transfer activities of PDZD8 are required for LE/lys positioning and neurite outgrowth

We next investigated the role of PDZD8 in the LE/lys positioning since PDZD8 interacted with Rab7 and protrudin, both of which have been shown to play essential roles in facilitating LE/lys anterograde trafficking (Raiborg et al., 2015a). We used siRNA-mediated suppression to explore the cellular functions of PDZD8. So far there is no effective commercial PDZD8 antibody for either western blots or immunofluorescence staining, and thus we used quantitative PCR (qPCR) to confirm the efficiency of PDZD8 suppression in COS7 or U2OS cells (Fig. S7A). We found that suppression of PDZD8 resulted in LE/lys clustering at perinuclear regions in comparison with scrambled siRNA-treated cells (Fig. 7A). The definition of perinuclear regions of cells is demonstrated in Fig. S7B. Besides COS7 cells, PDZD8 suppression led to more LE/lys clustering at perinuclear regions in multiple cell lines including U2OS (Fig. S7C,E) and HeLa (Fig. S7D,E) cells.

We further investigated whether the role of PDZD8 in LE/lys positioning was dependent on its lipid transfer activities. We made two lipid transfer-deficient mutants on the basis of full-length PDZD8 – a space-filling SMP mutant of PDZD8 (PDZD8-SMP-mut), in which the SMP domain of PDZD8 was replaced by the SMP V166W L285W mutant examined in Fig. 6D, and PDZD8-ΔSMP – for this purpose (Fig. 7B, top). The LE/lys positioning defects was near-completely rescued by siRNA-resistant full-length PDZD8–GFP (Fig. 7B,C). Although these two lipid transfer-deficient PDZD8 mutants were still able to mediate the formation of the ER–LE/lys MCSs, neither PDZD8-SMP-mut nor PDZD8-ΔSMP could rescue the LE/lys positioning defects (Fig. 7B,C), suggesting that lipid transfer activity of the SMP domain was essential for the positioning of LE/lys. In addition, we observed abnormally enlarged LE/lys upon expression of these two mutants in PDZD8-suppressed cells, suggesting that lipid transfer activity of PDZD8 is also required for other aspects of LE/lys including maturation, which agrees with a recent study showing that PDZD8 contributes to neuronal integrity (Shirane et al., 2020).

In addition, overexpression of protrudin promoted the anterograde transport of LE/lys, as revealed by the enrichment of Lamp1–Halo labeled LE/lys at cell periphery regions (Fig. S7F, top, yellow arrows). However, the defect of LE/lys positioning resulted from PDZD8 suppression was not substantially rescued by protrudin overexpression (Fig. S7F; Fig. 7C). This line of evidence indicates that PDZD8 is not functionally redundant to protrudin. Since these two proteins interacted with each other at MCSs, it is possible that PDZD8 is required in protrudin-mediated LE/lys anterograde transport because of the lipid transfer activities of PDZD8.

Since LE/lys anterograde transport promoted by protrudin-mediated MCSs is essential in neurite outgrowth (Raiborg et al., 2015a; Shirane and Nakayama, 2006), we further investigated whether PDZD8 played a role in the process of neurite outgrowth using PC12 cells (Black and Greene, 1982). Neuronal growth factor (NGF) stimulated PC12 differentiation, as revealed by the formation of extrusions with the length over >30 µm visualized by immunofluorescence staining of tubulin (Fig. 7D,E). Suppression of PDZD8 using lentivirus-encoded small hairpin RNAs (shRNAs) targeting PDZD8 significantly inhibited NGF-induced extrusion formation during PC12 differentiation (Fig. 7F). Both the percentage of cells with extensions longer than 30 µm and the length of extrusions substantially decreased upon PDZD8 shRNA treatment compared with that of scrambled shRNA-infected cells (Fig. 7F,K,L). The inhibition effects induced by PDZD8 suppression were comparable to that of protrudin suppression (Fig. 7G,K,L), whereas double suppression of protrudin and PDZD8 did not result in cumulative effects (Fig. 7H,K,L), supporting a hypothesis that PDZD8 and protrudin might function in a same pathway in neurite extension. The shRNA-mediated suppression of PDZD8 and protrudin were confirmed by qPCR (Fig. S7G). The expression of shRNA-resistant PDZD8–GFP substantially rescued the defects of neurite length in PDZD8-suppressed cells (Fig. 7I,K,L), but expression of the lipid transfer-deficient mutant PDZD8-SMP-mut did not substantially rescue this defect (Fig. 7J,K,L). This result indicates that lipid transfer activity of PDZD8 has an essential role in this process.

Journal of Cell Science (2022) 135, jcs255026. doi:10.1242/jcs.255026

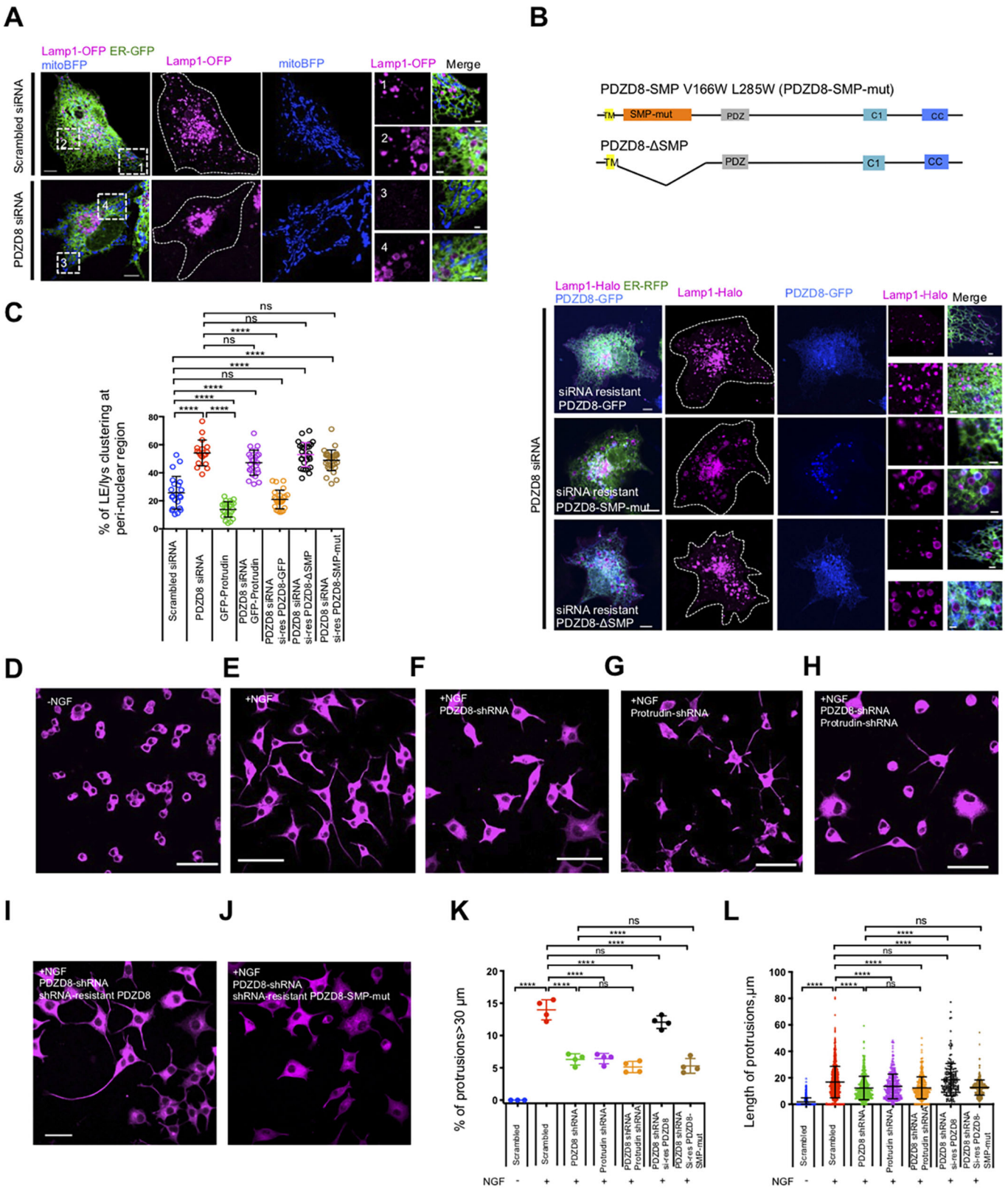

Fig. 7. See next page for legend.

DISCUSSION

Consistent with the recent studies, we demonstrated here that PDZD8 is a protrudin-interacting protein and acts as a tether at ER–LE/lys MCSs (Elbaz-Alon et al., 2020; Guillén-Samander et al., 2019; Hirabayashi et al., 2017; Shirane et al., 2020). Furthermore, we discovered that the SMP domain of PDZD8 binds glycerophospholipids and ceramides both *in vivo* and *in vitro*, and can transport lipids between membranes *in vitro*. Functionally,

Journal of Cell Science

Fig. 7. PDZD8 is required in LE/lys positioning and neurite outgrowth is dependent on the lipid transfer activity of SMP domain. (A) Representative confocal images of COS7 cells expressing Lamp1–OFP (magenta), ER-GFP (green) and mitoBFP (blue) upon treatments with scrambled (top) or PDZD8-specific siRNAs (bottom) with insets on the right. (B) Top, a diagram demonstrating two lipid transfer-deficient mutants of PDZD8. Bottom, representative confocal images of COS7 cells expressing Lamp1–Halo (magenta), ER-RFP (green) and siRNA-resistant PDZD8-GFP (top, blue), PDZD8-SMP-mut (middle, blue) or PDZD8-ΔSMP (bottom, blue) upon treatments with PDZD8 siRNAs. (C) Percentage of LE/lys at perinuclear regions in cells treated with scrambled (*n*=22) siRNA, PDZD8 siRNA (*n*=18), or with GFP–protrudin overexpression (*n*=24), GFP–protrudin overexpression and PDZD8 siRNA (*n*=25), siRNA-resistant PDZD8–GFP and PDZD8 siRNA (*n*=25), siRNA-resistant PDZD8-ΔSMP and PDZD8 siRNA (*n*=29) or siRNA-resistant PDZD8-SMP-mut and PDZD8 siRNA (*n*=32). All results were obtained from three independent experiments. ****P<0.0001; ns, not significant (ordinary one-way ANOVA with Tukey's multiple comparisons test). Mean±s.d. (D–J) Representative confocal images of fixed PC12 cells upon treatments with DMSO (D, *n*=495), NGF (E, *n*=666), NGF and PDZD8 shRNAs (F, *n*=412), NGF and protrudin shRNA (G, *n*=324), NGF and protrudin, and PDZD8 shRNAs (H, *n*=346), NGF and PDZD8 shRNA with siRNA-resistant PDZD8–GFP (I, *n*=193) or NGF and PDZD8 shRNAs with siRNA-resistant PDZD8-SMP-mut (J, *n*=368) in immunofluorescence stainings with anti-tubulin antibody. (K,L) Percentage of neurites with length over 30 µm (K) and the length of neurite extrusions (L). For quantifications, all data were obtained from three independent experiments. ****P<0.0001; ns, not significant (ordinary one-way ANOVA with Tukey's multiple comparisons test). Mean±s.d. Scale bars: 10 µm (whole-cell images in A,B); 30 µm (D–J); 2 µm (enlarged images A,B).

PDZD8 is required for LE/lys positioning and neurite growth in a lipid transfer activity-dependent manner.

It has been a mystery whether there are homologs of yeast ERMES, a complex that tethers the ER to mitochondria, in metazoans (Kornmann et al., 2009). A previous work proposed that PDZD8 was a functional ortholog of maintenance of mitochondrial morphology protein 1 (Mmm1) of yeast ERMES and that it acts to mediate the formation of the ER–mitochondria MCSs in mammalian cells based on domain-swapping assays along with complementation assays (Hirabayashi et al., 2017). However, domain-swapping and complementation experiments were insufficient to demonstrate that these two proteins (or even the domains) were functional orthologs, and PDZD8 and Mmm1 were more likely to be paralogs based on phylogenetic analyses (Wideman et al., 2018).

Our results, in accordance with recent studies from other groups (Elbaz-Alon et al., 2020; Guillén-Samander et al., 2019; Shirane et al., 2020), pointed to PDZD8 being a key player at ER-LE/lys MCSs. However, ER, LE/lys and mitochondria are physically associated, rendering it difficult to rule out the possible localizations and/or roles of PDZD8 in mitochondrially associated MCSs (Elbaz-Alon et al., 2020). In addition, a recent work by Kumar and Leonzino et al. revealed that VPS13A acts as a tether and LTP at ER–mitochondria MCSs (Kumar et al., 2018). VPS13A showed a clear and robust localization at ER–mitochondria MCSs in animal cells. VPS13A targets to ER through binding to VAP via its FFAT motif at the N terminus, while it recognizes mitochondria through C-terminal regions. Interestingly, a recent study demonstrated that VPS13A localizes at the interface between two types of mitochondrially associated MCSs – ER–mitochondria and mitochondria–endosome MCSs. VPS13A interacts with Rab7 on LE/lys and is required for efficient lysosomal degradation, suggesting an important role of VPS13A in crosstalk of these two different membrane contacts. Given that a complex homologous to ERMES was unlikely to be present in animal cells, VPS13A, but not PDZD8, might carry out the same roles as yeast ERMES and perform lipid transfer functions at such MCSs.

A growing number of studies have shown that many intracellular LTPs mediate lipid transport between opposing membranes at MCSs through two modes of action – shuttling or bridging. Shuttle transporters typically extract one or two lipid molecules from the membrane of the donor organelle, solubilize it during transport through the cytosol and deposit it in the acceptor organelle membrane, while bridge transporters feature an extended channel, most likely lined with hydrophobic residues that bind tens of lipids at once (Berrak et al., 2020; Lees and Reinisch, 2020; Louise et al., 2019).

It has been reported that a complex of multiple SMP domains shuttle glycerophospholipids across MCSs. For the SMP domain-containing protein E-Syt2, which transfers a range of glycerophospholipids between the ER and the plasma membrane, its shuttle mode of action was strongly supported because the dimer formed by its SMP domains was too short to bridge the gap between the membranes (Schauder et al., 2014). Another example is the SMP-containing transmembrane protein 24 (TMEM24; also known as C2CD2L), which is a shuttle transporter selective for phosphatidylinositols over other phospholipids. The crystal structure of TMEM24 shows that the lipid cavities of the two monomers do not join together at the head-to-head dimer interface, and therefore, lipids cannot flow along the length of the dimer (Lees et al., 2017). Similar to E-Syt2 and TMEM24, our results showed that PDZD8 forms dimers or oligomers through the SMP domain (Fig. S6F). More importantly, we showed that the SMP domain efficiently mediated glycerophospholipid (NBD-PC) and ceramide transport *in vitro* but its lipid-extracting activities in reactions with donor liposomes and without acceptor liposomes were very low (Fig. 6I,J). This result suggests that the SMP domain of PDZD8 extracts a very small amount of lipids from the membrane of donor liposomes, similar to what occurs with E-Syt1 (Kumar et al., 2018; Saheki et al., 2016; Valverde et al., 2019; Yu et al., 2016). This line of evidence supports that the SMP domain of PDZD8 adopts the shuttle model. In contrast, the chorein-N family of lipid transporters, including the Vps13 proteins and the autophagy-related protein Atg2, which feature an extended channel, bind tens of lipids at once and show much higher lipid extracting activities than E-Syt1 were reported to be bridge lipid transporters (Kumar et al., 2018; Li et al., 2020; Valverde et al., 2019). Therefore, our results suggest that PDZD8 might be a glycerophospholipid and ceramide shuttle transporter at ER–LE/lys MCSs. The crystal structure of the PDZD8-SMP domain is needed to confirm this hypothesis.

Our results show that the SMP domain of PDZD8 is capable of transporting PE *in vitro* lipid via transfer assays (Fig. 6K) in which a NBD–Rhodamine fluorescence donor–acceptor FRET pair was used. The unavailability of commercial Rhodamine-labeled lipids (such as Rh-cholesterol, Rh-PC or Rh-ceramide) has hampered our investigations of whether the PDZD8-SMP transports PC or ceramide. Although other red dyes (such as BODIPY TR)-labeled lipids are available, these red dye-labeled lipids were not suitable for the measurement (Redfern and Gericke, 2004). For instance, the excitation and emission of BODIPY-TR (589 nm/617 nm) are different from Rhodamine (558 nm/575 nm), suggesting that the BODIPY-TR may not be excited by the NBD (ex/em: 460 nm/534 nm) in FRET-based assays. Therefore, the lipid transfer activities of the PDZD8-SMP on PC or ceramide remain unclear and warrant further investigations.

Our results indicate that PDZD8 interacts and colocalizes with protrudin, which was previously shown to promote LE/lys anterograde transport (Raiborg et al., 2015a). We showed that these two proteins marked the same type of ER-LE/lys MCSs (Fig. 1C), and suppression of PDZD8 resulted in LE/lys clustering

Journal of Cell Science (2022) 135, jcs255026. doi:10.1242/jcs.255026

at perinuclear regions, which is similar to the phenotype found in protrudin-suppressed cells (Fig. 7A–C; Fig. S7B–D). Interestingly, protrudin is one of the ER–LE/lys MCSs tethers without lipid transport abilities, which raises a question of whether PDZD8 and protrudin might cooperate to regulate the LE/lys transport under certain physiological events, for example, in neurite outgrowth, in which a large number of LE/lys are required to transport to cell periphery. In this scenario, PDZD8 and protrudin have independent roles at the ER-LE/lys MCSs, with protrudin mediating efficient loading of LE/lys with kinesin-1 while PDZD8 transports lipids between ER and LE/lys at such MCSs, both of which are required for proper LE/lys positioning.

MATERIALS AND METHODS

Plasmids and siRNA and shRNA oligonucleotides

Human PDZD8-Myc-Flag was purchased from Origene (RC205601). PDZD8–GFP and all of the truncated PDZD8 mutants used in this study were generated by PCR amplifying human PDZD8-Myc-Flag (Origene, RC205601) and cloning it into mGFP-N1 (Addgene 54767). All of the constructs used in this study were generated by using ClonExpress®II One Step Cloning kit (Vazyme, C112-01). PDZD8-Halo was generated by inserting PDZD8 (RC205601) into Halo-N1, generated by replacing GFP with Halo in mGFP-N1 vector. pLVX-EF1α-PDZD8-GFP was generated by inserting PDZD8 into pLVX-EF1α-acGFP-N1 vector (Clontech, 631983). GST-C1-CC was generated by PCR amplifying the C1-CC region of PDZD8 (RC205601), and cloning into pGEX-2T, a gift from Hongjun Yu [Huazhong University of Science and Technology (HUST), China]. GST–SMP was generated by PCR amplifying the SMP region of PDZD8 (RC205601), and cloning into pGEX-2T. The SMP-mut (V166W; L258W) construct was generated by site-directed mutagenesis, and the GST-SMP-mut was generated by PCR amplifying the SMP-mut, and cloning into pGEX-2T. The tethered SMP-His construct was made according to the process described in Kumar et al. (2018) with modifications. Briefly, PDZD8 (88–294) containing the SMP lipid transport domain was fused to the PH domain of rat PLCΔ (11–140) and cloned into a pSec-tag2A vector containing a C-terminal His_6 tag, a gift from Hongjun Yu (HUST, China). EGFP–protrudin was a gift from Camilla Raiborg (University of Oslo, Norway). All of the truncated Flag–protrudin mutants used in this study were generated by PCR, amplifying specific regions of human EGFP–protrudin, and cloning them into Flag-C1 vectors. Site-directed mutagenesis was used to generate seven silent mutations per siRNA seed region in PDZD8–GFP, creating siRNA-resistant PDZD8–GFP mRNA that translates into wild-type PDZD8–GFP. The siRNA-resistant PDZD8-ΔSMP–GFP mutant was constructed by PCR amplification of siRNA-resistant PDZD8–GFP with primers that excluded the SMP domain. The siRNA-resistant PDZD8-SMP-mut–GFP was constructed by insertion of PCR amplified SMP-mut into siRNA-resistant PDZD8-ΔSMP-GFP. mCherry-Rab5a, pTY-CR-hRab7A, pTY-CR-hRab7A(Q67L) and pTY-CR-hRab7A(T22N) were gifts from Yueguang Rong (HUST, China). Dox-inducible PCW-Flag-Rab7A was generated by inserting Rab7 into the PCW vector (Addgene 89180). ER–mGFP, ER-tagRFP and mitoBFP were previously described (Ji et al., 2017). Lamp1–OFP was HG11215-ACR (Sino Biological Inc. Beijing, China). Lamp1–Halo was generated by inserting Lamp1 (HG11215-ACR) into Halo-N1. psPAX (Addgene 12260), pMD2.G (Addgene 12259), GFP-Mapper (Addgene 117721), were bought from Addgene. All oligonucleotides for suppressing gene expression were synthesized by RiboBIO (Guangzhou, China).

PDZD8-shRNA (Rat) against target sequence (5′-AAGATCAGGTTT-AAGCCGTTT-3′) was cloned into PLKO.1-TCR (Addgene 10878). Protrudin-shRNA (Rat) against target sequence (5′-AAGCTTCTTG-ATC-CGACTGGA-3′) was cloned into PLKO.1-TCR (Addgene 10878). PDZD8 siRNAs were against target sequences: 5′-GCACAAGTGTCAAAACCAA-3′ (siRNA#1); 5′-CCATGTAGTTACTAACGTA-3′ (siRNA#2); 5′-GCCA-ACTAATAGACTCTCA-3′ (siRNA#3). Protrudin siRNAs were against target sequences: 5′-TCTGCATGCTGTATTTGCT -3′ (siRNA#1); 5′-CCTCGTGTAACCAGACCTT-3′ (siRNA#2); 5′-CCACCTTCTCAGTGC-TGAA-3′ (siRNA#3); RAB7a siRNAs were against target sequences: 5′-CAACGAATTTCCTGAACCT-3′ (siRNA#1); 5′-GAGCTGACTTTCTG-ACCAA-3′ (siRNA#2); 5′-CCAGACGATTGCACGGAAT-3′ (siRNA#3); VPS37B siRNAs were against target sequences: 5′-GGTTCTCTTTGAAG-CCTAT-3′ (siRNA#1); 5′-GCTGGACACGTTGAAAGCA-3′ (siRNA#2); 5′-GGAGACCCTGTTAGCACTT-3′ (siRNA#3). As a control, scrambled siRNA/shRNA 5′-CGUUAAUCGCGUAUAAUACGCGUAT-3′ was used.

Cell culture and transient transfection

The African green monkey kidney fibroblast-like COS7 cell line (ATCC), human osteosarcoma U2OS cells (ATCC), human cervical cancer HeLa cells (ATCC), human embryonic kidney 293T (ATCC) and mouse neuroblastoma Neuro-2a cells (ATCC) were grown in DMEM (Invitrogen) supplemented with 10% fetal bovine serum (Gibco). The rat pheochromocytoma PC12 cell line were grown in RPMI1640 (Invitrogen) supplemented with 10% horse serum (Gibco) and 5% fetal bovine serum (Gibco). All of the cell lines used in this study were confirmed free of mycoplasma contamination.

For transfection, cells were seeded at 4×10^5 cells per well in a six-well dish ∼16 h before transfection. Plasmid transfections were performed in OPTI-MEM (Invitrogen) with 2 µl Lipofectamine 2000 per well for 6 h, followed by trypsinization and replating onto glass-bottom confocal dishes at ∼3.5×10^5 cells per well. Cells were imaged in live-cell medium (DMEM with 10% FBS and 20 mM Hepes with no penicillin or streptomycin) ∼16–24 h after transfection. For all transfection experiments in this study, the following amounts of DNA were used per 3.5 cm well (individually or combined for co-transfection): 500 ng for PDZD8–GFP, mito-BFP, GFP-Mapper, Lamp1–Halo and Lamp1–OFP; 1000 ng for ER-tagRFP and ER-mGFP; 300 ng for pTY-CR-hRab7A, pTY-CR-hRab7A(Q67L) and pTY-CR-hRab7A(T22N). For siRNA transfections, cells were plated on 3.5 cm dishes at 30–40% density, and 2 µl Lipofectamine RNAimax (Invitrogen) and 50 ng siRNA were used per well. At 48 h after transfection, a second round of transfection was performed with 50 ng siRNAs. Cells were analyzed 24 h after the second transfection for suppression.

Generation of the stable pLVX-EF1α-PDZD8-GFP COS7 cell line and Dox-inducible PCW-Flag-Rab7 / pLVX-EF1α-PDZD8-GFP COS7 cell line

To generate the pLVX-EF1α-PDZD8-GFP COS7 cell line, on day 1, 293T cells were seeded into a 10 cm dish with ∼3×10^6 cells 18 h before transfection. On day 2, transfections were performed with 4 µg pLVX-EF1α-PDZD8-GFP, 3 µg psPAX2 and 2 µg pMD2.G. On day 3, COS7 cells were seeded onto 10 cm dishes with 2×10^6 cells per dish. On day 4, the supernatant from transfected 293T cells was collected (48 h post initial transfection), followed by filtering through a syringe with 0.22 µm filter. Then 1 ml filtered 293T supernatant was added to the COS7 cells. On day 5, COS7 cells were grown in puromycin-containing (1 µg/ml) medium, and then were verified by imaging and western blots. The procedure for generating the Dox-inducible PCW-Flag-Rab7 and pLVX-EF1α-PDZD8-GFP COS7 cell line is similar to that for the stable pLVX-EF1α-PDZD8-GFP COS7 cell line except that virus-infected COS7 cells were grown in G418 (2 µg/ml) medium. For induction, DOX (2 µg/ml) was added to medium, and cells were verified by imaging and western blots 48 h post-infection.

Antibodies and reagents

Anti-GFP (AE011, ABclonal), anti-protrudin (A15943, ABclonal), anti-Flag (F1804 sigma), anti-His (2366 CST), anti-Rab7a (A12784, ABclonal), anti-tubulin (100109-MM05T, Sinobiological), anti-GST (AE027, ABclonal), anti-Rab5 (A12304, ABclonal) were used at 1:5000 for western blots and 1:100 dilution for immunofluorescence. Janilia Fluo® 646 HaloTag® Ligand (Promega, GA112A) was added to complete medium in concentration of 20 nM, followed by incubation for 15 min. Cells were washed with PBS twice before imaging. Cells were treated with 10 µM wortmannin (T6283, TargetMol) in complete medium overnight. Cells were treated with 1 µM VPS34-IN1 (T7015, TargetMol) in complete medium for 6 h. Lipids were purchased from Avanti Polar Lipids as follows: NBD-PC (810133), NBD-PE (810144), Rh-PE (810150), NBD-PS (810198), NBD-PA (810138), NBD-ceramide (810211) and NBD-Cholesterol (810252).

Journal of Cell Science (2022) 135, jcs255026. doi:10.1242/jcs.255026

Live imaging by confocal microscopy

Cells were grown on 35 mm glass-bottom confocal MatTek dishes. Confocal dishes were loaded to a laser scanning confocal microscope (LSM780, Zeiss, Germany) equipped with multiple excitation lasers (405 nm, 458 nm, 488 nm, 514 nm, 561 nm and 633 nm) and a spectral fluorescence GaAsP array detector. Cells were imaged with the 63×1.4 NA iPlan-Apochromat 63× oil objective using the 405 nm laser for BFP, 488 nm for GFP, 561nm for mStrawberry, OFP, tagRFP or mCherry and 633nm for Janilia Fluo® 646 HaloTag® Ligand.

Live cell super-resolution Lattice-SIM microscopy

Cells were grown on 35 mm glass-bottom confocal MatTek dishes, and medium was changed to OptiMEM prior to loading to Elyra Lattice SIM (Zeiss, Germany). Super-resolution lattice-SIM images were acquired on Elyra 7 with Lattice SIM equipped with a 63×/1.4 NA Plan-Apochromat oil immersion objective, 405, 488, 561 and 642 nm lasers and sCMOS cameras (PCO.Edge CLHS). Cells were imaged with the 405 nm laser for BFP, 488 nm for GFP, 561 nm for tagRFP and 642 nm for Janilia Fluo® 646 HaloTag® Ligand. Images were subsequently processed using the Zen software. The end images had the resolution of 120 nm in *X*-*Y* and 300 nm in *Z*.

Immunofluorescence staining

Cells were fixed with 4% paraformaldehyde (PFA, Sigma) in PBS for 10 min at room temperature. After washing with PBS three times, cells were permeabilized with 0.1% Triton X-100 in PBS for 15 min on ice. Cells were then washed three times with PBS, blocked with 1% FBS in PBS for 1 h, incubated with primary antibodies in diluted blocking buffer overnight, and washed with PBS three times. Secondary antibodies were applied for 1 h at room temperature. After washing with PBS three times, samples were mounted on Vectashield (H-1000; Vector Laboratories).

Quantitative RT-PCR for detecting mRNA level of PDZD8

Cells were transfected with either scrambled, PDZD8 siRNA/shRNA or protrudin siRNA/shRNA. At 4 days after transfection, RNA was isolated with Trizol (ThermoFisher) according to the manufacturer's instructions. cDNA was reverse transcribed using RverTra Ace (TRT-101, TOYOBO) according to the directions of the manufacturer. The cDNA was analyzed using quantitative PCR with qPCR Mix (QPS-201, TOYOBO) using the following primers for quantifications of PDZD8 mRNA levels in U2OS and COS7 cells: h-GAPDH: 5′-TCATTGACCTCAACTACATGGTTT-3′; 5′-GAAGATGGTGATGGGATTTC-3′; GAPDH Chlorocebus sabaeus: 5′-TGAAGGTCGGAGTCAACGG-3′; 5′-TGGGTGGAATCATACTGGAA-CA-3′; PDZD8: 5′-GTCCGCCTACTTGTTTGTCAA-3′; 5′-CACCTCG-AAGTCGATCAGCG-3′; and the following primers for quantifications of PDZD8 and protrudin mRNA levels in PC12 cells: actin: 5′-AGGGAAA-TCGTGCGTGAC-3′; 5′-CGGAACCGCTCATTGCCG-3′; PDZD8: 5′-G-CCTCTTTGTGGAGCGACTG-3′; 5′-TGATATGCCTTGTCAACCCT-3′; protrudin: 5′-AAGATGCAATAGAGGAGGACG-3′; 5′-GTTGTTGG-TCGGGTAGCG-3′.

GFP-trap assay

GFP trap (GTA-100, ChromoTek) was used for detection of proten–protein interactions and the GFP-Trap assays were performed according to the manufacturer's protocol. 5% input was used in GFP traps unless otherwise indicated.

Mass spectrometry for identifications of GFP–protrudin- or PDZD8–GFP-interacting proteins

The bound proteins were extracted from IP beads using SDT lysis buffer (4% SDS, 100 mM DTT, 100 mM Tris-HCl pH 8.0). IP beads sample were boiled for 3 min and further ultrasonicated. Undissolved beads were removed by centrifugation at 16,000 ***g*** for 15 min. The supernatant, containing proteins, were collected. Protein digestion was performed with FASP method. Briefly, the detergent, DTT and IAA in UA buffer was added to block-reduced cysteine. Finally, the protein suspension was digested with 2 µg trypsin (Promega) overnight at 37°C. The peptide was collected by centrifugation at 16,000 ***g*** for 15 min. The peptide was desalted with C18 StageTip for further LC-MS analysis. LC-MS/MS experiments were performed on a Q Exactive Plus mass spectrometer that was coupled to an Easy nLC (Thermo Fisher Scientific). Peptide was first loaded to a trap column (100 µm×20 mm, 5 µm, C18, Dr Maisch GmbH, Ammerbuch, Germany) in buffer A (0.1% formic acid in water). Reverse-phase high-performance liquid chromatography (RP-HPLC) separation was performed using a self-packed column (75 µm×150 mm; 3 µm ReproSil-Pur C18 beads, 120 Å, Dr Maisch GmbH, Ammerbuch, Germany) at a flow rate of 300 nl/min. The RP-HPLC mobile phase A was 0.1% formic acid in water, and B was 0.1% formic acid in 95% acetonitrile. The gradient was set as following: 2%–4% buffer B from 0 min to 2 min, 4% to 30% buffer B from 2 min to 47 min, 30% to 45% buffer B from 47 min to 52 min, 45% to 90% buffer B from 52 min and to 54 min, and 90% buffer B kept until to 60 min. MS data was acquired using a data-dependent top20 method dynamically choosing the most abundant precursor ions from the survey scan (350–1800 *m*/*z*) for HCD fragmentation. A lock mass of 445.120025 Da was used as internal standard for mass calibration. The full MS scans were acquired at a resolution of 70,000 at *m*/*z* 200, and 17,500 at *m*/*z* 200 for MS/MS scan. The maximum injection time was set to 50 ms for MS and 50 ms for MS/MS. Normalized collision energy was 27 and the isolation window was set to 1.6 Th. Dynamic exclusion duration was 60 s. The MS data were analyzed using MaxQuant software version 1.6.1.0. MS data were searched against the UniProtKB *Rattus norvegicus* database (36,080 total entries, downloaded 08/14/2018). Trypsin was seleted as the digestion enzyme. A maximum of two missed cleavage sites and the mass tolerance of 4.5 ppm for precursor ions and 20 ppm for fragment ions were defined for database search. Carbamidomethylation of cysteines was defined as a fixed modification, while acetylation of protein N-terminal, oxidation of Methionine were set as variable modifications for database searching. The database search results were filtered and exported with a <1% false discovery rate (FDR) at peptide-spectrum-matched level, and protein level, respectively.

Mass spectrometry for identification of PDZD8–GFP- and PDZD8-SMP-associated lipids

Mass spectrometry for identification of PDZD8–GFP- and PDZD8-SMP-associated lipids was performed as follows. To extract lipids, 1 ml methyl tert-butyl ether (MTBE) was added to GFP-Trap agarose beads (Chromoteck) and the samples were shaken for 1 h at room temperature. Next, phase separation was induced by adding 250 µl water, letting it sit for 10 min at room temperature and centrifuging for 15 min at 14,000 ***g***, 4°C. Because of the low density and high hydrophobicity of MTBE, lipids and lipophilic metabolites are mainly extracted to the upper MTBE-rich phase. The lipid was transferred to fresh tubes and dried with nitrogen.

Additionally, to ensure data quality for metabolic profiling, quality control (QC) samples were prepared by pooling aliquots from representative samples for all of the analysis samples, and were used for data normalization. QC samples were prepared and analyzed with the same procedure as that for the experiment samples in each batch. Dried extracts were then dissolved in 50% acetonitrile. Each sample was filtered with a disposable 0.22 µm cellulose acetate and transferred into 2 ml HPLC vials and stored at −80°C until analysis. For UHPLC-MS/MS analysis, lipid analysis was performed on Q Exactive orbitrap mass spectrometer (Thermo Fisher Scientific) coupled to a UHPLC system Ultimate 3000 (Thermo Fisher Scientific). Samples were separated using a Hypersil GOLD C18 column (100×2.1 mm, 1.9 µm) (Thermo Fisher Scientific). Mobile phase A was prepared by dissolving 0.77 g of ammonium acetate to 400 ml of HPLC-grade water, followed by adding 600 ml of HPLC-grade acetonitrile. Mobile phase B was prepared by mixing 100 ml of acetonitrile with 900 ml isopropanol. The flow rate was set as 0.3 ml/min. The gradient was 30% B for 0.5 min and was linearly increased to 100% in 10.5 min, and then maintained at 100% in 2 min, and then reduced to 30% in 0.1 min, with 4.5 min re-equilibration period employed. Both electrospray ionization (ESI) positive-mode and negative-mode were applied for MS data acquisition. The positive mode of spray voltage was 3.0 kV and the negative mode 2.5 kV. The ESI source conditions were set as follows: heater temperature of 300°C, Sheath Gas Flow rate, 45arb, Aux Gas Flow Rate, 15 arb, Sweep Gas Flow Rate, 1arb, Capillary Temp, 350°C, S-Lens RF Level,

50%. The full MS scans were acquired at a resolution of 70,000 at *m/z* 200, and 17,500 at *m/z* 200 for MS/MS scans. The maximum injection time was set to for 50 ms for MS and 50 ms for MS/MS. MS data was acquired using a data-dependent Top10 method dynamically choosing the most abundant precursor ions from the survey scan (200–1500 *m/z*) for HCD fragmentation. Stepped normalized collision energy was set as 15, 25, 35 and the isolation window was set to 1.6 Th. QC samples were prepared by pooling aliquots that were representative of all samples under analysis, and used for data normalization. Blank samples (75% acetonitrile in water) and QC samples were injected every six samples during acquisition.

For data preprocessing and filtering, lipids were identified and quantified using LipidSearch 4.1.30 (Thermo, CA). Mass tolerance of 5 ppm and 10 ppm were applied for precursor and product ions. Retention time shift of 0.25 min was performed in 'alignment'. M-score and chromatographic areas were used to reduce false positives. The lipids with less than 30% relative standard deviation (RSD) of MS peak area in the QC samples were kept for further data analysis.

SIMCAP software (Version 14.0, Umetrics, Sweden) was used for all multivariate data analyses and modeling. Data were mean-centered using Pareto scaling. Models were built on principal component analysis (PCA), orthogonal partial least-square discriminant analysis (PLS-DA) and partial least-square discriminant analysis (OPLS-DA). All the models evaluated were tested for over fitting with methods of permutation tests. The descriptive performance of the models was determined by R2X (cumulative) [perfect model: R2X (cum)=1] and R2Y (cumulative) [perfect model: R2Y (cum)=1] values while their prediction performance was measured by Q2 (cumulative) [perfect model: Q2 (cum)=1] and a permutation test (n=200). The permuted model should not be able to predict classes – R2 and Q2 values at the *Y*-axis intercept must be lower than those of Q2 and the R2 of the non-permuted model. OPLS-DA allowed the determination of discriminating metabolites using the variable importance on projection (VIP). The VIP score value indicates the contribution of a variable to the discrimination between all the classes of samples. Mathematically, these scores are calculated for each variable as a weighted sum of squares of PLS weights. The mean VIP value is 1, and usually VIP values over 1 are considered as significant. A high score is in agreement with a strong discriminatory ability and thus constitutes a criterion for the selection of biomarkers.

The discriminating metabolites were obtained using a statistically significant threshold of variable influence on projection (VIP) values obtained from the OPLS-DA model and two-tailed Student's *t*-test (*P*-value) on the normalized raw data at univariate analysis level. The *P*-value was calculated by one-way analysis of variance (ANOVA) for multiple groups analysis. Metabolites with VIP values greater than 1.0 and *P*-value less than 0.05 were considered to be statistically significant metabolites. Fold change was calculated as the logarithm of the average mass response (area) ratio between two arbitrary classes. On the other side, the identified differential metabolites were used to perform cluster analyses with R package.

GST-tag protein purification

GST constructs were transformed into *Escherichia coli* BL21 (DE3) cells, and cells were incubated at 37°C until the optical density (OD) at 600 nm reached 0.6–0.8. Subsequently, cells were incubated at 16°C for another hour, followed by induction with 1 mM IPTG overnight at 16°C. Cells were lysed via sonication. GST fusion proteins were purified via the GST-tag Protein Purification kit (P2262, Beyotime, China), followed by size-exclusion chromatography (GE Healthcare) with protein standard mix (69385, Sigma) according to the manufacturer's instructions.

Pulldown assays

Purified GST–C1-CC and GST was incubated with 20 µl Glutathione resin (P2262, Beyotime, China) at 4°C overnight, followed by washing beads with freshly prepared HNM buffer (20 mM Hepes, pH 7.4, 0.1 M NaCl, 5 mM $MgCl_2$, 1 mM DTT and 0.2% NP-40). Purified His–Rab7 (80629-R07E, Sinobiological Inc.) or Rab5 (PRO-590, Prospec) was incubated with 100 µM GTP or GDP at 25°C for 30 min, followed by addition of 30 mM $MgCl_2$ and incubation at 25°C for another 1 h. Finally, GTP or GDP-loaded His–Rab7 or Rab5 was subjected to GST pulldown using GST–C1-CC or GST-only loaded glutathione resin overnight at 4°C, respectively. Glutathione resin was washed with freshly prepared HNM buffer. Glutathione resin was re-suspended in 100 µl 2× SDS-sampling buffer. Re-suspended resin was boiled for 10 min at 95°C to dissociate protein complexes from beads. Western blotting was performed using anti-His antibodies and anti-Rab5 antibodies. The Coomassie staining was performed for purified GST-C1-CC and GST, with His–Rab7 and Rab5 as loading controls.

In vitro lipid-binding assay

1 µl of either NBD-labeled PE, PS, PA, PC, cholesterol or ceramide (1 mg/ml in methanol) was incubated with 19 µl purified GST-SMP, purified GST-SMP mutant or purified GST-C1-CC (1 mg/ml) for 2 h at 4°C. Samples were visualized on 10% native PAGE gels. NBD fluorescence was visualized using Bio-Rad ChemiDoc XRS+170-8265, and comigrated with protein was visualized with Coomassie staining.

Protein purification of tethered PDZD8-SMP–His

The tethered-SMP–His constructs were transfected into 10-cm dishes of HEK293T cells, and the medium was changed 5 h later. After another 24 h, cells were incubated in OptiMEM. Medium was collected 48 h later, and centrifuged at 500 ***g*** for 10 min.The supernatant was mixed with 500 µl of balanced HisPur™ Ni-NTA Resin (88221, Thermo Scientific) and incubated in a 4°C shaking bed for 2 h. After centrifugation at 1000 ***g*** for 10 min, the supernatant was discarded. Proteins on beads were washed with 20 mM Tris-HCl pH 8.0, 300 mM NaCl buffer containing 20 mM, 50 mM, 100 mM, and 200 mM imidazole in turn. The eluted proteins were examined by Coomassie staining and western blotting experiments. Then, the eluted proteins were concentrated (Millipore UFC900396), and washed with imidazole-free buffer to obtain the imidazole-free and concentrated tethered-SMP–His proteins.

In vitro FRET-based lipid-transfer assay

Lipid transfer experiments were performed in 100 µl volumes in 96-well plates containing a protein: lipid ratio of 1:800, with 0.25 µM protein, 100 µM donor liposomes [61% DOPC, 30% liver PE, 2% NBD-PC/ceramide, 2% Rhodamine-PE, and 5% DGS-NTA(Ni)] and 100 µM acceptor liposomes [65% DOPC, 30% liver PE and 5% PI(4,5P)2]. The fluorescence intensity of NBD was measured via excitation at 460 nm and detection at 538 nm every 0.5 min for 15 min at 30°C using a CLARIOstar Plus Microplate Reader (BMG LABTECH). All data were normalized to the NBD fluorescence at first time point (t=0).

Dithionite assay

After performing a lipid-transfer reaction (as described above), 2.5 µl freshly prepared dithionite buffer (100 mM dithionite in 50 mM Tris-HCl pH 10) was added to reactions, and NBD fluorescence was monitored for an additional 15 min.

Liposome pull-down assay

For the liposome pull-down assay, proteins were diluted to 7 µg/ml in osmotically matched protein dilution buffer (20 mM Hepes, 120 mM NaCl, 1 mM EGTA, 0.2 mM $CaCl_2$, 1.5 mM $MgCl_2$, 1 mM DTT, 5 mM KCl, pH 7.4, 1% BSA was added to enhance solubility) and were pre-cleared by ultracentrifugation at 120,000 ***g*** for 45 min using a TLA100.3 rotor in a Beckmann Optima-MAX benchtop ultracentrifuge. 1 ml of protein mixture was then combined with 10 µl of liposomes and incubated with shaking at 30°C. Liposomes were recovered by ultracentrifugation (120,000 ***g*** for 30 min); supernatant and pellet fractions were resuspended in equal volumes of 1× Laemmli buffer and analyzed by western blots.

Dynamic light scattering assay

For the DLS measurements, a Litesizer 500 (Anton Paar) with a semiconductor laser (40 mW, 658 nm) was used. For each sample, three independent runs of 10 s were performed according to the manufacturer's instruction. Measurements were made at 25°C.

Image analysis for quantification of frequency or number of PDZD8-decorated LE/lys and quantification of the positioning of LE/lys

All image analysis and processing was performed using ImageJ (National Institutes of Health). The number of PDZD8-decorated LE/lys was counted manually with assistance of ImageJ plugin 'Cell counter'. PDZD8-decorated LE/lys represents the LE/lys that are completely coated by PDZD8. For quantification of LE/lys positioning, perinuclear regions of cells were defined as shown in Fig. S7B. To calculate the percentage of perinuclearly LE/lys, we manually counted the number of total LE/lys and perinuclearly LE/lys with the assistance of an ImageJ plugin Cell counter.

Analysis of neurite outgrowth in PC12 cells

Rat pheochromocytoma PC12 cells were grown in RPMI1640 (Invitrogen) supplemented with 10% horse serum (Gibco) and 5% fetal bovine serum (Gibco). PC12 cells were infected using Polybrene overnight before NGF (100 ng/ml) stimulation for 48 h. Cells were subjected to immunofluorescence stainings using anti-tubulin antibodies. The length and number of neurites were measured manually with ImageJ.

Statistical analysis

All statistical analyses and *P*-value determinations were performed in GraphPad Prism6. To determine *P*-values, an ordinary one-way ANOVA with Tukey's multiple comparison tests was performed among multiple groups. A two-tailed unpaired Student's *t*-tests was performed between two groups of data. The error bars in plots represent mean±s.d.

Acknowledgements

We thank Camilla Raiborg (Oslo University) for protrudin constructs. We thank Anbing Shi (Huazhong University of Science and Technology, China), Yugang Wang (Huazhong University of Science and Technology) and Lin Deng (Shenzhen Bay Institute, CN) for discussions and reagents; we thank Ke Tang (Huazhong University of Science and Technology) for technical assistance on FACS, Hongjun Yu (Huazhong University of Science and Technology) for assistance on protein expression and purification. We also thank Guangjun Cai (Huazhong University of Science and Technology) and Jia Wang (Shanghai Bioprofile Technology Company Ltd.) for technical support on imaging and mass spectrometry, respectively.

Competing interests

The authors declare no competing or financial interests.

Author contributions

Conceptualization: Y.G., J.X., Q.-Z.C., W.-K.J.; Methodology: Y.G., J.X., Q-Z.C., W.-K.J.; Software: Y.G., J.X., Q-Z.C., W.-K.J.; Validation: Y.G., J.X., Q-Z.C., W.-K.J.; Formal analysis: Y.G., J.X., Q-Z.C., W.-K.J.; Investigation: Y.G., J.X., Q-Z.C., W.-K.J.; Resources: Y.G., J.X., Q-Z.C., W.-K.J.; Data curation: Y.G., J.X., Q-Z.C., W.-K.J.; Writing - original draft: Y.G., J.X., Q-Z.C., W.-K.J.; Writing - review & editing: Y.G., J.X., Q-Z.C., W.-K.J.; Visualization: Y.G., J.X., Q-Z.C., W.-K.J.; Supervision: W.-K.J.; Project administration: W.-K.J.; Funding acquisition: J.X., W.-K.J.

Funding

The work was supported by National Natural Science Foundation of China (91854109; 31701170; 81901166), and the Program for HUST Academic Frontier Youth Team (grant 2018QYTD11).

Peer review history

The peer review history is available online at https://journals.biologists.com/jcs/article-lookup/DOI/10.1242/jcs.255026/

References

Alpy, F., Rousseau, A., Schwab, Y., Legueux, F., Stoll, I., Wendling, C., Spiegelhalter, C., Kessler, P., Mathelin, C., Rio, M.-C. et al. (2013). STARD3 or STARD3NL and VAP form a novel molecular tether between late endosomes and the ER. *J. Cell Sci.* **126**, 5500-5512. doi:10.1242/jcs.139295

Berrak, U., William, H.-C., Marianna, L. and Pietro, D. C. (2020). Role of VPS13, a protein with similarity to ATG2, in physiology and disease. *Curr. Opin. Genet. Dev.* **65**, 61-68. doi:10.1016/j.gde.2020.05.027

Black, M. M. and Greene, L. A. (1982). Changes in the colchicine susceptibility of microtubules associated with neurite outgrowth: studies with nerve growth factor-responsive PC12 pheochromocytoma cells. *J. Cell Biol.* **95**, 379-386. doi:10.1083/jcb.95.2.379

Chang, C.-L., Hsieh, T.-S., Yang, T. T., Rothberg, K. G., Azizoglu, D. B., Volk, E., Liao, J.-C. and Liou, J. (2013). Feedback regulation of receptor-induced Ca2+ signaling mediated by E-Syt1 and Nir2 at endoplasmic reticulum-plasma membrane junctions. *Cell Rep.* **5**, 813-825. doi:10.1016/j.celrep.2013.09.038

Cohen, S., Valm, A. M. and Lippincott-Schwartz, J. (2018). Interacting organelles. *Curr. Opin. Cell Biol.* **53**, 84-91. doi:10.1016/j.ceb.2018.06.003

Eden, E. R., White, I. J., Tsapara, A. and Futter, C. E. (2010). Membrane contacts between endosomes and ER provide sites for PTP1B-epidermal growth factor receptor interaction. *Nat. Cell Biol.* **12**, 267-272. doi:10.1038/ncb2026

Elbaz-Alon, Y., Guo, Y., Segev, N., Harel, M., Quinnell, D. E., Geiger, T., Avinoam, O., Li, D. and Nunnari, J. (2020). PDZD8 interacts with Protrudin and Rab7 at ER-late endosome membrane contact sites associated with mitochondria. *Nat. Commun.* **11**, 3645. doi:10.1038/s41467-020-17451-7

Fidler, D. R., Murphy, S. E., Courtis, K., Antonoudiou, P., El-Tohamy, R., Ient, J. and Levine, T. P. (2016). Using HHsearch to tackle proteins of unknown function: a pilot study with PH domains. *Traffic* **17**, 1214-1226. doi:10.1111/tra.12432

Friedman, J. R., DiBenedetto, J. R., West, M., Rowland, A. A. and Voeltz, G. K. (2013). Endoplasmic reticulum-endosome contact increases as endosomes traffic and mature. *Mol. Biol. Cell* **24**, 1030-1040. doi:10.1091/mbc.e12-10-0733

Gatta, A. T. and Levine, T. P. (2017). Piecing together the patchwork of contact sites. *Trends Cell Biol.* **27**, 214-229. doi:10.1016/j.tcb.2016.08.010

Guillén-Samander, A., Bian, X. and De Camilli, P. (2019). PDZD8 mediates a Rab7-dependent interaction of the ER with late endosomes and lysosomes. *Proc. Natl. Acad. Sci. USA* **116**, 22619-22623. doi:10.1073/pnas.1913509116

Hirabayashi, Y., Kwon, S. K., Paek, H., Pernice, W. M., Paul, M. A., Lee, J., Erfani, P., Raczkowski, A., Petrey, D. S., Pon, L. A. et al. (2017). ER-mitochondria tethering by PDZD8 regulates Ca(2+) dynamics in mammalian neurons. *Science* **358**, 623-630. doi:10.1126/science.aan6009

Hönscher, C. and Ungermann, C. (2014). A close-up view of membrane contact sites between the endoplasmic reticulum and the endolysosomal system: from yeast to man. *Crit. Rev. Biochem. Mol. Biol.* **49**, 262-268. doi:10.3109/10409238.2013.875512

Hoyer, M. J., Chitwood, P. J., Ebmeier, C. C., Striepen, J. F., Qi, R. Z., Old, W. M. and Voeltz, G. K. (2018). A novel class of ER membrane proteins regulates ER-associated endosome fission. *Cell* **175**, 254-265.e14. doi:10.1016/j.cell.2018.08.030

Hurley, J. H. and Misra, S. (2000). Signaling and subcellular targeting by membrane-binding domains. *Annu. Rev. Biophys. Biomol. Struct.* **29**, 49-79. doi:10.1146/annurev.biophys.29.1.49

Ji, W.-K., Chakrabarti, R., Fan, X., Schoenfeld, L., Strack, S. and Higgs, H. N. (2017). Receptor-mediated Drp1 oligomerization on endoplasmic reticulum. *J. Cell Biol.* **216**, 4123-4139. doi:10.1083/jcb.201610057

King, C., Prabuddha, S., Seo, A. Y. and Lippincott-Schwartz, J. (2020). ER membranes exhibit phase behavior at sites of organelle contact. *Proc. Natl. Acad. Sci. USA* **117**, 7225-7235. doi:10.1073/pnas.1910854117

Kornmann, B., Currie, E., Collins, S. R., Schuldiner, M., Nunnari, J., Weissman, J. S. and Walter, P. (2009). An ER-mitochondria tethering complex revealed by a synthetic biology screen. *Science* **325**, 477-481. doi:10.1126/science.1175088

Kumar, N., Leonzino, M., Hancock-Cerutti, W., Horenkamp, F. A., Li, P., Lees, J. A., Wheeler, H., Reinisch, K. M. and De Camilli, P. (2018). VPS13A and VPS13C are lipid transport proteins differentially localized at ER contact sites. *J. Cell Biol.* **217**, 3625-3639. doi:10.1083/jcb.201807019

Lees, J. A. and Reinisch, K. M. (2020). Inter-organelle lipid transfer: a channel model for Vps13 and chorein-N motif proteins. *Curr. Opin. Cell Biol.* **65**, 66-71. doi:10.1016/j.ceb.2020.02.008

Lees, J. A., Messa, M., Sun, E. W., Wheeler, H., Torta, F., Wenk, M. R., De Camilli, P. and Reinisch, K. M. (2017). Lipid transport by TMEM24 at ER-plasma membrane contacts regulates pulsatile insulin secretion. *Science* **355**, eaah6171. doi:10.1126/science.aah6171

Li, P., Lees, J. A., Lusk, C. P. and Reinisch, K. M. (2020). Cryo-EM reconstruction of a VPS13 fragment reveals a long groove to channel lipids between membranes. *J. Cell Biol.* **219**, e202001161. doi:10.1083/jcb.202001161

Louise, H., Alberto, T. G. and Tim, P. L. (2019). Lipid transfer proteins: the lipid commute via shuttles, bridges and tubes. *Nat. Rev. Mol. Cell Biol.* **20**, 85-101. doi:10.1038/s41580-018-0071-5

Meers, P., Ali, S., Erukulla, R. and Janoff, A. S. (2000). Novel inner monolayer fusion assays reveal differential monolayer mixing associated with cation-dependent membrane fusion. *Biochim. Biophys. Acta.* **1467**, 227-243. doi:10.1016/S0005-2736(00)00224-8

Murphy, S. E. and Levine, T. P. (2016). VAP, a versatile access point for the endoplasmic reticulum: review and analysis of FFAT-like motifs in the VAPome. *Biochim. Biophys. Acta* **1861**, 952-961. doi:10.1016/j.bbalip.2016.02.009

Phillips, M. J. and Voeltz, G. K. (2016). Structure and function of ER membrane contact sites with other organelles. *Nat. Rev. Mol. Cell Biol.* **17**, 69-82. doi:10.1038/nrm.2015.8

Raiborg, C., Wenzel, E. M., Pedersen, N. M., Olsvik, H., Schink, K. O., Schultz, S. W., Vietri, M., Nisi, V., Bucci, C., Brech, A. et al. (2015a). Repeated ER-endosome contacts promote endosome translocation and neurite outgrowth. *Nature* **520**, 234-238. doi:10.1038/nature14359

Raiborg, C., Wenzel, E. M. and Stenmark, H. (2015b). ER-endosome contact sites: molecular compositions and functions. *EMBO J.* **34**, 1848-1858. doi:10.15252/embj.201591481

Redfern, D. A. and Gericke, A. (2004). Domain formation in phosphatidylinositol monophosphate/phosphatidylcholine mixed vesicles. *Biophys. J.* **86**, 2980-2992. doi:10.1016/S0006-3495(04)74348-9

Reinisch, K. M. and De Camilli, P. (2016). SMP-domain proteins at membrane contact sites: Structure and function. *Biochim. Biophys. Acta* **1861**, 924-927. doi:10.1016/j.bbalip.2015.12.003

Rowland, A. A., Chitwood, P. J., Phillips, M. J. and Voeltz, G. K. (2014). ER contact sites define the position and timing of endosome fission. *Cell* **159**, 1027-1041. doi:10.1016/j.cell.2014.10.023

Saheki, Y. and De Camilli, P. (2017). Endoplasmic reticulum-plasma membrane contact sites. *Annu. Rev. Biochem.* **86**, 659-684. doi:10.1146/annurev-biochem-061516-044932

Saheki, Y., Bian, X., Schauder, C. M., Sawaki, Y., Surma, M. A., Klose, C., Pincet, F., Reinisch, K. M. and De Camilli, P. (2016). Control of plasma membrane lipid homeostasis by the extended synaptotagmins. *Nat. Cell Biol.* **18**, 504-515. doi:10.1038/ncb3339

Schauder, C. M., Wu, X., Saheki, Y., Narayanaswamy, P., Torta, F., Wenk, M. R., De Camilli, P. and Reinisch, K. M. (2014). Structure of a lipid-bound extended synaptotagmin indicates a role in lipid transfer. *Nature* **510**, 552-555. doi:10.1038/nature13269

Scorrano, L., De Matteis, M. A., Emr, S., Giordano, F., Hajnoczky, G., Kornmann, B., Lackner, L. L., Levine, T. P., Pellegrini, L., Reinisch, K. et al. (2019). Coming together to define membrane contact sites. *Nat. Commun.* **10**, 1287. doi:10.1038/s41467-019-09253-3

Shirane, M. and Nakayama, K. I. (2006). Protrudin induces neurite formation by directional membrane trafficking. *Science* **314**, 818-821. doi:10.1126/science.1134027

Shirane, M., Wada, M., Morita, K., Hayashi, N., Kunimatsu, R., Matsumoto, Y., Matsuzaki, F., Nakatsumi, H., Ohta, K., Tamura, Y. et al. (2020). Protrudin and PDZD8 contribute to neuronal integrity by promoting lipid extraction required for endosome maturation. *Nat. Commun.* **11**, 4576. doi:10.1038/s41467-020-18413-9

Truebestein, L. and Leonard, T. A. (2016). Coiled-coils: the long and short of it. *BioEssays* **38**, 903-916. doi:10.1002/bies.201600062

Valm, A. M., Cohen, S., Legant, W. R., Melunis, J., Hershberg, U., Wait, E., Cohen, A. R., Davidson, M. W., Betzig, E. and Lippincott-Schwartz, J. (2017). Applying systems-level spectral imaging and analysis to reveal the organelle interactome. *Nature* **546**, 162-167. doi:10.1038/nature22369

Valverde, D. P., Yu, S., Boggavarapu, V., Kumar, N., Lees, J. A., Walz, T., Reinisch, K. M. and Melia, T. J. (2019). ATG2 transports lipids to promote autophagosome biogenesis. *J. Cell Biol.* **218**, 1787-1798. doi:10.1083/jcb.201811139

van der Kant, R. and Neefjes, J. (2014). Small regulators, major consequences - Ca(2)(+) and cholesterol at the endosome-ER interface. *J. Cell Sci.* **127**, 929-938. doi:10.1242/jcs.137539

van der Kant, R., Zondervan, I., Janssen, L. and Neefjes, J. (2013). Cholesterol-binding molecules MLN64 and ORP1L mark distinct late endosomes with transporters ABCA3 and NPC1. *J. Lipid Res.* **54**, 2153-2165. doi:10.1194/jlr.M037325

Wideman, J. G., Balacco, D. L., Fieblinger, T. and Richards, T. A. (2018). PDZD8 is not the 'functional ortholog' of Mmm1, it is a paralog. *F1000Res* **7**, 1088. doi:10.12688/f1000research.15523.1

Wong, L. H., Copic, A. and Levine, T. P. (2017). Advances on the Transfer of Lipids by Lipid Transfer Proteins. *Trends Biochem. Sci.* **42**, 516-530. doi:10.1016/j.tibs.2017.05.001

Wu, H., Carvalho, P. and Voeltz, G. K. (2018). Here, there, and everywhere: the importance of ER membrane contact sites. *Science* **361**, eaan5835. doi:10.1126/science.aan5835

Yu, H., Liu, Y., Gulbranson, D. R., Paine, A., Rathore, S. S. and Shen, J. (2016). Extended synaptotagmins are Ca2+-dependent lipid transfer proteins at membrane contact sites. *Proc. Natl. Acad. Sci. USA* **113**, 4362-4367. doi:10.1073/pnas.1517259113

Zajac, A. L., Goldman, Y. E., Holzbaur, E. L. and Ostap, E. M. (2013). Local cytoskeletal and organelle interactions impact molecular-motor- driven early endosomal trafficking. *Curr. Biol.* **23**, 1173-1180. doi:10.1016/j.cub.2013.05.015